OXFORD

Journal of Petrology, 2025, **66**, egaf094
https://doi.org/10.1093/petrology/egaf094
ADVANCE ACCESS PUBLICATION DATE 11 NOVEMBER 2025
Original Manuscript

Olivines Fo-Ni-MnO Systematics in the Trans-Mexican Volcanic Belt: Evidence for Cool and Silicic Primary Arc Magmas

SUSANNE M. STRAUB[1], VALENTINA BATANOVA[2], ALEXANDER SOBOLEV[2], ARTURO GÓMEZ-TUENA[3], RAMON ESPINASA-PERENA[4], ILYA N BINDEMAN[5], FINLAY M. STUART[6], ELISABETH WIDOM[7] and YOSHIYUKI IIZUKA[8]

[1]Lamont Doherty Earth Observatory at the Columbia University, 61 Route 9W, Palisades, NY 10964, USA
[2]Univ. Grenoble Alpes, Univ. Savoie Mont Blanc, CNRS, IRD, Univ. Gustave Eiffel, ISTerre, 38000 Grenoble, France
[3]Instituto de Geologia, Universidad Nacional Autónoma de México, 04360 Ciudad de México, Coyoacán, CDMX, Mexico
[4]Instituto de Geologia, Investigación Científica, Copilco Universidad, 04360 Ciudad de México, Coyoacán, CDMX, Mexico
[5]Department of Earth Sciences, University of Oregon, Eugene, OR 97403-1272, USA
[6]Isotope Geosciences Unit, Scottish Universities Research and Reactor Centre, East Kilbride G75 0QF, UK
[7]Department of Geology and Environmental Earth Science, Miami University, 118 Shideler Hall, 250 S. Patterson Ave., Oxford, OH 45056, USA
[8]Institute of Earth Sciences, Academia Sinica, 128 Academia Road, Sec. 2, Nangang, Taipei 11529, Taiwan, ROC

*Corresponding author. Telephone: +845 365 8464. Fax: +845 365 8155. E-mail: smstraub@ldeo.columbia.edu

The discovery of systematic differences in the trace element composition of forsteritic olivines in primitive magmas from within-plate, arc and mid-ocean ridge volcanoes engendered much debate about a causal link to the recycling of oceanic crust into the mantle sources of within-plate and arc magmas. Here we address this problem using Cr-spinel bearing, forsteritic (~$Fo_{80–91}$) olivines from high-Mg# = 50 = 73 [Mg# = molar ratio of Mg/(Mg + Fe^{2+})*100] arc magmas from the Trans-Mexican Volcanic Belt (TMVB). The TMVB arc front olivines have similar high Ni, low MnO, and low Mn/Fe as forsteritic olivines from within-plate basalts erupting through thick lithosphere (= WPB-thick). However, the olivines in TMVB arc front primary melts crystallize at much lower temperatures of T^{oliv}_{cryst}~1119 ± 38 °C (calculated with olivine–spinel aluminum exchange thermometry) in hydrous (~4–9 wt % H_2O), silicic, less magnesian (≤10 wt % MgO) mantle melts from mostly garnet-free mantle sources. Model calculations suggest that the primary arc front melts last equilibrated in the mantle at pressures of ~1.4 to ~1.9 GPa (~51–69 km depth) and low temperatures (T_{source} = 1150 ± 45 °C) that are only slightly higher than the olivine crystallization temperatures. While the $Kd^{Ni}_{oliv/melt}$ increases in the cooler and silicic melts, such modulation cannot account for the full range of Ni concentration in TMVB magmatic olivines. A small population of very high-Ni olivines (>4000–5500 μg/g Ni) is best explained by crystallization in Ni-rich components melt that formed by melt rock reaction processes in the mantle wedge. Unlike Ni, olivine MnO is not sensitive to melt temperature and only moderately to melt composition, and thus retains mantle source characteristics. In the TMVB, olivine Fo-MnO-Mn/Fe systematics record an ambient mantle wedge (= mantle without slab component) that is similar to WPB sources and that is variably depleted by slab flux-driven melt extraction. Overall, the olivine Fo-Ni-MnO systematics confirm with greater detail than possible by bulk rock studies that the TMVB primary melts are hydrous and silicic and originate from a mantle wedge that is strongly and variably modified by the slab flux. These results reaffirm a strong genetic link between slab recycling and the genesis of silicic arc magmas.

Key words: arc magmas; chromian spinel; melt temperature; olivine; trace elements

INTRODUCTION

The discovery of systematic differences in the olivine Fo ratio [which is the molar ratio of Mg/(Mg + Fe^{2+})*100] and Ni and MnO concentrations in forsteritic olivines from within-plate basalts (WPB), mid-ocean ridge basalts (MORB), and arc volcanic rocks, has sparked much debate over if and how olivine Fo–Ni–MnO variations reflect the recycling of silicic components from subducted oceanic crust into the mantle. One group of models argues that such recycling is highly reactive and that it changes the lithology and composition of the peridotite mantle and its primary melts. Sobolev *et al.* (2005, 2007) first proposed the formation of olivine-free, secondary pyroxenite segregations, following the infiltration of silicic partial melts from deep-seated and ancient eclogite that locally transformed mantle olivine to pyroxenes. Secondary pyroxenites inherit the compatible elemental budget of the original peridotite, but have different partition coefficients and thus produce Ni-rich melts that crystallize magmatic olivines with high Ni, lower MnO and Mn/Fe. Soon after, Wang & Gaetani (2008) showed experimentally that high-Ni olivines do not require the formation of secondary pyroxenites. They propose that the percolating silicic eclogite melts assimilate by reactive dissolution elements Mg, Fe (at a constant Fe/Mg), and Ni from the surrounding mantle peridotite. Because the olivine/melt partition coefficients, $Kd^{Ni}_{oliv/melt}$, increase exponentially with increasing melt polymerization (Hart & Davis, 1978; Beattie *et al.*, 1991; Wang & Gaetani, 2008), the modified silicic melt can then crystallize

RECEIVED FEBRUARY 24, 2025; **REVISED** OCTOBER 31, 2025

high-Ni olivines despite only moderate Ni concentrations of ~200–300 μg/g.

More recently, an alternative group of models argues that the observed olivine Fo-Ni-MnO variations in WPB were unrelated to lithological change or melt–rock reaction processes in the mantle source. Instead, they were due to the modulation of the olivine/melt partition coefficients by concomitant changes of melt pressure and temperature, in addition to accessory mantle phases like garnet (Putirka *et al.*, 2011; Matzen *et al.*, 2017; Yu & Langmuir, 2023). Matzen *et al.* (2013) showed experimentally that the $Kd^{Ni}_{oliv/melt}$ increases as temperature decreases. The $Kd^{Ni}_{oliv/melt}$ is low at the high temperatures and pressures in the mantle source but increases with decreasing melt temperatures and pressures in adiabatically rising mantle melts. Matzen *et al.* (2013) argue that ΔT, the temperature difference between the mantle source (T_{source}) and surface ($T_{surface}$) ($\Delta T = T_{source} - T_{surface}$), can be large enough to sufficiently increase $Kd^{Ni}_{oliv/melt}$ for crystallizing high-Ni magmatic olivines in within-plate basalts erupting through thick lithosphere (= WPB-thick), which start melting at high pressures of ~4–4.5 GPa. In their model, the MnO is retained in residual garnet in the deep WPB-thick mantle sources (Matzen *et al.*, 2017). Yu & Langmuir (2023) confirmed and refined this model, and showed it to be compatible with the uptake of a low-degree eclogite melt in the source that accounts for the major and trace element composition of the WPBs, but does not affect the olivine trace chemistry.

High-Ni olivines from WPB have received the most attention to date, yet they are also reported from several volcanic arcs (e.g. Straub *et al.*, 2008, 2011*b*; Bryant *et al.*, 2011; Díaz-Bravo *et al.*, 2014; Gordeychik *et al.*, 2018; Pu *et al.*, 2024). Primary arc magmas originate from a mantle wedge that absorbs silicic slab components (fluids, melts, and diapirs). Experiments suggest that their infiltration in the wedge peridotite is reactive and promotes the formation of pyroxenes at the expense of olivine (e.g. Mallik *et al.*, 2015, 2016; Codillo *et al.*, 2018; Lara & Dasgupta, 2020; Rebaza Morillo *et al.*, 2023). Thus, high-Ni arc olivines have been linked to the presence of secondary pyroxenites in the mantle wedge (e.g. Straub *et al.*, 2008, 2011*b*; Ruprecht & Plank, 2013; Gómez-Tuena *et al.*, 2018). However, hydrous primary arc magmas are also cooler, less magnesian, and more silicic than primary melts of mid-ocean ridge and within-plate settings, despite similar high-melt Mg#s [=molar ratio of $Mg/(Mg+Fe^{2+})*100$] of >60 (Mitchell & Grove, 2015; Schmidt & Jagoutz, 2017; Till, 2017; Lara & Dasgupta, 2020). The experimental data (e.g. Matzen *et al.*, 2017; Yu & Langmuir, 2023) predict that the composition- and temperature-sensitive $Kd^{Ni}_{oliv/melt}$ are higher in such magmas, and crystallize forsteritic olivine with higher Ni concentrations. Thus, the question arises whether high-Ni arc olivines simply reflect variations in the composition and temperature of the primary melts instead of melt/rock reaction processes in the mantle wedge.

To reassess the potential of olivine trace elements Ni and MnO as tracers of mantle wedge processes, we revisited the high-Ni olivines in the continental Trans-Mexican Volcanic Belt (TMVB) that had been used previously to argue for secondary pyroxenite formation in the mantle wedge (e.g. Straub *et al.*, 2008, 2011*b*, 2013, 2014). These olivines are forsteritic (~$Fo_{80–91}$) and Cr-spinel bearing, as typical for their crystallization in primitive mantle-derived melts. The olivines and their bulk rocks are well investigated, including bulk rock major and trace elements and Sr-Nd-Pb-Hf-Os isotope ratios, and olivine major and trace elements (Ni, Ca) and He-O-Os isotope ratios (e.g. Straub *et al.*, 2023; Ahmadi *et al.*, 2025). Collectively, these data constrain melt origin from a mantle wedge that has been strongly modified by slab additions and that experienced no, or negligible, crustal contamination (e.g. Straub *et al.*, 2015, 2023; Ahmadi *et al.*, 2025). In this study, we add (1) new high-precision olivine MnO data for better comparison with the Fo-Ni-MnO systematics of the WPB-olivines (Matzen *et al.*, 2017; Yu & Langmuir, 2023), and (2) olivine-Cr-spinel crystallization temperatures obtained from olivine–spinel aluminum exchange thermometry (OSAT) (Coogan *et al.*, 2014; Zhang *et al.*, 2023) to assess the influence of melt temperature on olivine/melt partitioning. We then investigate how integrating the temperature dependence of the $Kd^{Ni}_{oliv/melt}$ affects the evidence for melt–rock reaction processes in the TMVB mantle wedge and discuss the implications for petrogenetic models.

GEOLOGICAL SETTING AND SAMPLES

The TMVB is an active Quaternary volcanic arc that is linked to the subduction of young oceanic crust of the Cocos and Rivera plates at the Middle American Trench (Fig. 1). Detailed reviews of the TMVB are provided by Gómez-Tuena *et al.* (2018, 2007). In short, the TMVB has a broad, irregular arc front that is marked by nine major composite volcanoes and several monogenetic fields that are constructed on a ~35- to 50-km-thick continental basement that varies in composition and age (Proterozoic to Cenozoic). The TMVB is well known for the abundance of olivine-phyric basalt to andesite magmas that can have high Mg# (up to 73) and MgO concentrations (up to 10 wt %). Most TMVB magmas are 'calc-alkaline' based on a SiO_2-FeO/MgO discrimination diagram (Miyashiro, 1974), and display strongly fractionated incompatible element patterns with relative Nb-Ta depletions (Nb ~3–16 μg/g), and enrichments in large-ion-lithophile elements (LILE). Calc-alkaline magmas construct the composite volcanoes and dominate in the monogenetic fields. A calc-alkaline variety are the rare monogenetic 'high-K' magmas that have even stronger Nb-Ta depletions, are enriched in light rare earth elements (REE), and exhibit the steep heavy REE patterns indicative of residual garnet in the source (e.g. Gómez-Tuena *et al.*, 2011; Straub *et al.*, 2013, 2014). A second important monogenetic group is the OIB-type (ocean island basalts) arc magmas, which have high Nb (>16–36 μg/g) concentrations and minimally fractionated incompatible trace element patterns similar to those of intraplate magmas (e.g. Straub *et al.*, 2015). The OIB-type arc magmas are often considered primitive melts from mantle wedge domains that are least modified by the subduction flux (e.g. Wallace & Carmichael, 1999; Blatter *et al.*, 2007; Gómez-Tuena *et al.*, 2018). They form a compositional continuum with the calc-alkaline/high-K magmas, and many magmas of either series have transitional major and trace element compositions.

The TMVB study areas

The samples for this study come from two locations at the arc volcanic front and one location at the TMVB rear-arc (Fig. 1).

Popocatépetl/SCVF

This is the principal arc front location which comprises the composite volcano Popocatépetl and the westerly adjacent monogenetic Sierra Chichinautzin Volcanic Field (SCVF). Popocatépetl/SCVF volcanoes erupt ~90 km above the slab (Perez-Campos *et al.*, 2008) and through ~45-km-thick crust composed of Paleozoic high-grade metamorphic complexes of the Mixteco terrane (Gómez-Tuena *et al.*, 2018). The volcanic vents of the samples studied here are located within an arc front-parallel segment of only ~70 km length and ~10 km width (Fig. 1). Here, monogenetic calc-alkaline, high-K, and OIB-type magmas erupt within a few

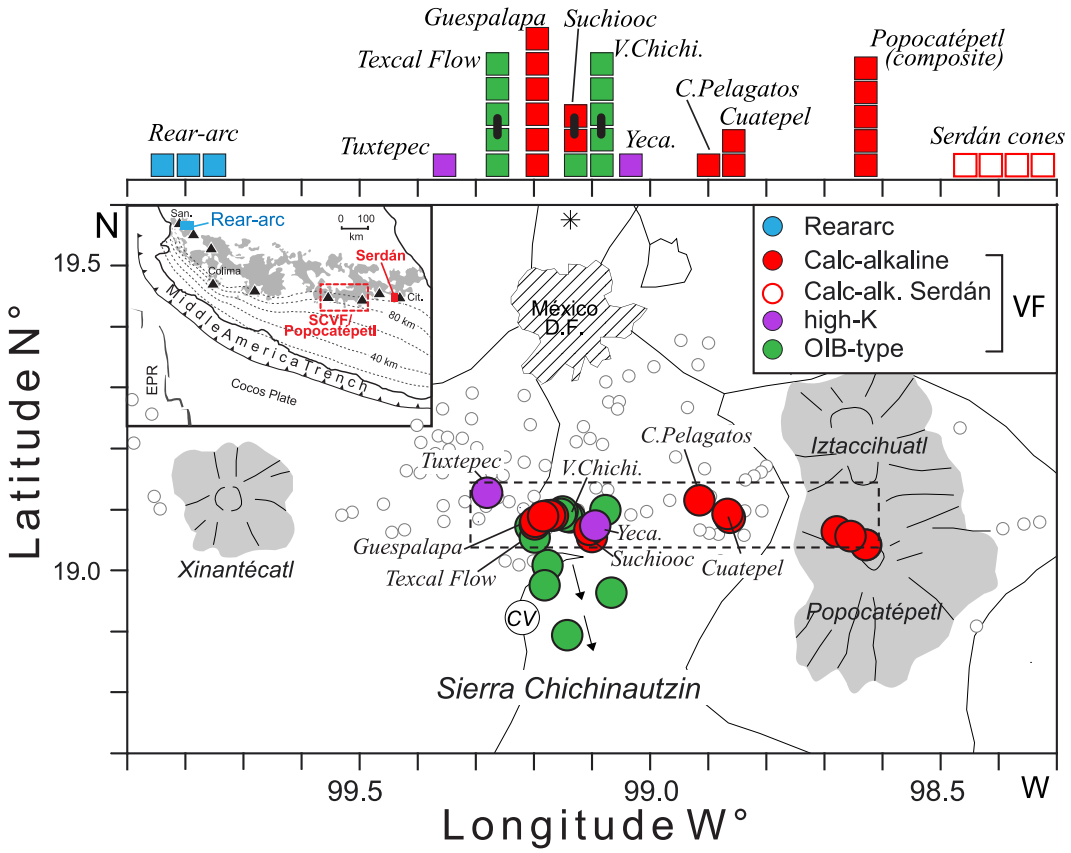

Fig. 1. Map of the Trans-Mexican Volcanic Belt. Inset: Trans-Mexican Volcanic Belt (gray-shaded) with nine quaternary composite volcanoes (black triangles); Sangangüey (= San) and Colima are named. Stippled rectangle inset denotes Popocatépetl/Sierra Chichinautzin Volcanic Field; squares denote the location of the Serdán and rear-arc basalts, respectively. Slab surface contours (stippled) after Pardo & Suarez (1995). EPR, East Pacific Rise. Enlargement: Close-up of Popocatépetl/Sierra Chichinautzin Volcanic Field with monogenetic volcanoes (open small circles) between composite volcanoes Xinantécatl and Popocatépetl-Iztaccihuatl. Filled circles—sample locations. Stippled rectangle (c. 10 × 70 km) denotes a zone of volcanic vents, which produce up to ~10–20-km-long lavas flowing downhill to the south (arrows). Italic names—denote monogenetic volcanoes sampled. V. Chichi.—Volcan Chichinautzin, Yeca.—Yecahuazac. CV—City of Cuernavaca. Colored boxes on top illustrate number of eruptive units sampled from individual volcanoes, which are mostly non-co-genetic except when connected by a black bar.

kilometers of each other, and sometimes from the same vent (Straub *et al.*, 2014). All volcanic rocks studied are of Pleistocene and Holocene age, and they comprise (1) 16 calc-alkaline basalts to dacites [MgO ~3.4–9.7 wt %; Mg# ~60–68; up to 207 μg/g Ni]; (2) two high-K basalts and basaltic andesites [MgO ~8.0–9.7 wt %; Mg# ~70–73; up to 220 μg/g Ni]; and (3) 11 OIB-type arc magmas [MgO ~3.2–8.2 wt %; Mg# ~51–67; up to 180 μg/g Ni].

Serdán basalts

The second arc front location is located ~122 km to the east of the Popocatépetl/SCVF in the foothills of Citlaltepetl near the town of Serdán. The four 'Serdán basalts' are from four Pleistocene monogenetic volcanoes that erupt high-Mg# basalts and basaltic andesites [MgO ~8.2–9.4 wt %; Mg# ~68–71; up to 182 μg/g Ni] within ~15 km from each other. The Serdán basalts erupt >100 to ~200 km above the slab through c. 35- to 40-km-thick continental crust of possibly Precambrian age (Gómez-Tuena *et al.*, 2018). They serve to test the validity of the olivine variations of the Popocatépetl/SCVF group within the broader TMVB.

Rear-arc basalts

The four rear-arc basalts [MgO ~5.8–9.2 wt %; Mg# ~55–68; up to 192 μg/g Ni] are from four Plio-Pleistocene monogenetic, high-TiO_2 volcanoes from the vicinity (~10–20 km) of the Sangangüey composite volcano (~104.7° W). They erupt through ~40-km-thick continental crust not older than the late Triassic, are located >320 km above the slab, and lack subduction signatures (e.g. Gómez-Tuena *et al.*, 2018). Rear-arc basalts were included because they may represent magmas from a TMVB-type mantle before its advection to arc front and subduction modification (Díaz-Bravo *et al.*, 2014; Gómez-Tuena *et al.*, 2014; Straub *et al.*, 2023).

Selection of samples for olivine studies

The 37 samples selected are identical to those that Straub *et al.* (2023) used for a study of olivine CaO and Cr-spinel inclusions. Most samples are not co-genetic, having distinct bulk rock Sr-Nd-Pb-Hf isotopes and/or incompatible trace element ratios. Some samples are from different volcanoes, and others from the same volcano (Fig. 1) (e.g. Straub *et al.*, 2013, 2014). Most samples (33) are from arc front volcanoes (5 from Popocatépetl, 23 samples from 9 monogenetic volcanoes of the Sierra Chichinautzin Volcanic Field, and 4 Serdán basalts), and four samples are from the rear-arc. For convenience, the previously published bulk rock data are recompiled in Table S1.

At the arc front, Cr-spinel-bearing olivines (referred to as olivine+Cr-spinels hereafter) are mostly the only phenocrysts; some high-Mg# andesites have also high-Mg# orthopyroxene phenocrysts (Straub & Martin-Del Pozzo, 2001; Straub *et al.*, 2014). Clinopyroxene phenocrysts are absent, and plagioclase appears only in the most silica-rich OIB-type varieties. At Popocatépetl,

olivine+Cr-spinels are antecrysts in plagioclase- and pyroxene-phyric Popocatépetl dacites (e.g. Straub *et al.*, 2008, 2011*b*). The rear-arc basalts also crystallize plagioclases and clinopyroxene after the olivine+Cr-spinels (Díaz-Bravo *et al.*, 2014).

METHODS

Sample preparation and analytical methods

Full details of sample preparation and analytical methods were reported by Straub *et al.* (2023) and are reiterated in Supplement A. In short, individual olivine crystals were separated from crushed rock, mounted in distinct patterns in epoxy, and ground to expose olivine cores. This preparation avoids fluorescence effects on the olivine trace elements from surrounding materials (e.g. Gavrilenko *et al.*, 2023), and enables the repeat analysis of individual olivines.

Two sets of electron microprobe (EMP) data were collected with beam currents of 100 and 900 nA, respectively (see Supplement A for details). At 100 nA, typically 10–20 olivine crystals per sample were measured, which included first-order core-to-rim transects for each olivine (typically between 6 and 12 points per olivine) for identification and testing for zoning patterns. The 100 nA data for SiO_2, MgO, FeO, Ni, and CaO were previously reported (Straub *et al.*, 2008, 2011*b*, 2013, 2023); 100 nA data for olivine MnO are reported here for the first time.

Based on the 100 nA data, representative olivines for each sample were selected for paired olivine-Cr-spinel analyses using a 900 nA beam for the olivines. Typically, 2–4 olivine points were measured next to a single Cr-spinel inclusion that was analyzed once or twice. Cr-spinel data were reported by Straub *et al.* (2023). A total of 337 olivine-spinel pairs in 246 individual olivine phenocrysts in 36 samples was obtained (some phenocrysts have multiple olivine-spinel pairs). Cr-spinels in the center of the olivines were preferentially analyzed, and thus the 900 nA data do not record zoning. The 900 nA data for SiO_2, MgO, FeO, Ni, and CaO for 36 samples (minus rear-arc sample TPZ10–24) were previously reported by Straub *et al.* (2023); the 900 nA data for MnO, Al_2O_3, Cr_2O_3, TiO_2, Na_2O, and P_2O_5 are reported for the first time, as well as the results of olivine-spinel aluminum exchange thermometry. The olivine data are listed in Tables S2 and S3.

Olivine-spinel aluminum exchange thermometry

OSAT is ideal for arc magmas because it is not sensitive to meltwater or oxygen fugacity, and resistant to diffusive resetting owing to the slow diffusivity of Al and Cr (Coogan *et al.*, 2014; Zhang *et al.*, 2023). The OSAT crystallization temperatures (T^{Al}_{oliv}) were calculated with the Zhang *et al.* (2023) formula, which is calibrated for 1174–1606 °C and retrieves T^{Al}_{oliv} with method errors of either ±24 and ±43 °C (Table S4). The T^{Al}_{oliv} were calculated for the 246 individual olivine phenocrysts from the 36 samples, whereby the olivine and Cr-spinel composition for each olivine crystal is the average of all individual olivine-spinel pairs obtained for this olivine.

Most T^{Al}_{oliv} obtained for the TMVB olivine+Cr-spinels (89%) are below the calibration range of Zhang *et al.* (2023), but this is unlikely to affect their accuracy for several reasons. First, the composition of the TMVB Cr-spinels and olivines is mostly within the experimental calibration range. For Cr-spinel, this includes the Cr# [= molar Cr/(Cr + Al) ∗100], the atomic Ti (= Ti atoms per 4 O), and the Fe^{3+}/Fe^{tot} [= molar $Fe_2O_3/(Fe_2O_3 + FeO)$]; only two Cr-spinels have a higher atomic Ti, but their T^{Al}_{oliv} are inconspicuous. Most TMVB olivines used for OSAT thermometry have high Fo >84 (81% of the olivines) and have low P_2O_5 <0.05 wt % (85%) of the olivines used in the calibration; the T^{Al}_{oliv} of olivines with lower Fo <84 or higher P_2O_5 >0.05 wt % are not outlying. The higher melt SiO_2 activity is not expected to affect T^{Al}_{oliv}, as olivine Al^{3+} is most likely split between the M and T crystallographic sites (Coogan *et al.*, 2014). Second, as it will be discussed below, the T^{Al}_{oliv} match well with olivine crystallization temperatures (T^{oliv}_{cryst}) obtained after Pu *et al.* (2024) and Putirka (2008) for those samples for which olivine/melt equilibria could be established.

RESULTS

Olivine Fo-Ni-MnO systematics of TMVB olivines

A principal observation is that the TMVB arc front and rear-arc olivines differ in similar ways from each other as WPB-thick and MORB olivines differ (Figs 2 and 3). The TMVB arc front olivines resemble WPB-thick olivines, with similarly high Ni concentrations and lower MnO and Mn/Fe∗100 (Straub *et al.*, 2008, 2011*a*). They also display a similar inverse correlation in olivine MnO vs Ni space, albeit with greater variability. In contrast, the TMVB rear-arc olivines partially (MnO) or fully (Ni) overlap with MORB olivines.

A notable point is the deceptive similarity of the TMVB olivine trends to olivine-only 'crystal lines of descent', despite olivine-only fractional crystallization cannot create the observed olivine Fo-Ni and Fo-MnO trends (Straub *et al.*, 2023). This is because most of the olivines, which construct these trends, crystallize from non-co-genetic melts [denoted in Fig. 1, and detailed in Straub *et al.*, 2023]. In Fig. 2d–f, each filled colored circle represents the average composition of all olivines contained in a single non-co-genetic magma (Straub *et al.*, 2023); circles of the same color denote olivine averages from non-co-genetic magmas from the same volcano. The similarity to the olivine crystal lines of descents is especially striking in Fo-Mn space, where there is none of the individuality of the olivine trends in Fo-Ni space (Straub *et al.*, 2011*a*).

The comparison of TMVB vs WPB-thick olivines is robust since TMVB olivines are not influenced by very high or strongly variable melt oxidation states. The percentage of ferric Fe in the TMVB melts has previously been estimated to be 11 ± 2% with a range from 8 to 17%, based on the Fe^{3+}/Fe^{2+} ratio in Cr-spinel inclusions in olivine (Straub & Martin-Del Pozzo, 2001; Straub *et al.*, 2023). This percentage of ferric Fe is typical for arc magmas (Kelley & Cottrell, 2009), and is too low and limited to cause strong fractionations in olivine Fo or Mn/Fe.

Bulk rock variations of TMVB, MORB, and WPB-thick magmas

While TMVB and WPB-thick olivine Fo-Ni-MnO variations are similar, their bulk rock compositions starkly differ. In Fig. 4, WPB-thick magmas are exemplified by Hawaii [following Yu & Langmuir, 2023]. Collectively, at similar high Mg#s, the TMVB bulk rocks have lower FeO∗ ≤8 ∼wt %, MnO ≤0.15 wt %, MgO ≤ ∼10 wt %, and Ni ≤ ∼200 μg/g than the Hawaiian basalts that have FeO ∼11 wt %, MnO ∼0.17 wt %, MgO ∼14 wt %, and Ni ∼600 μg/g. The difference is lesser for the TMVB rear-arc and OIB-type arc magmas, and largest for the calc-alkaline/high-K magmas, which have the highest Mg# and SiO_2 (Fig. 4). Notably, TMVB bulk rock Ni and Mn/Fe are more comparable to MORB than to the Hawaiian basalts, despite a small offset to lower Mn/Fe relative to MORB (Fig. 4c).

Olivine-Cr-spinel crystallization temperatures

In their entirety, T^{Al}_{oliv} of the TMVB olivines range from 909 to 1244 °C (Figs 5 and 6). If three Popocatépetl olivines with outlying low

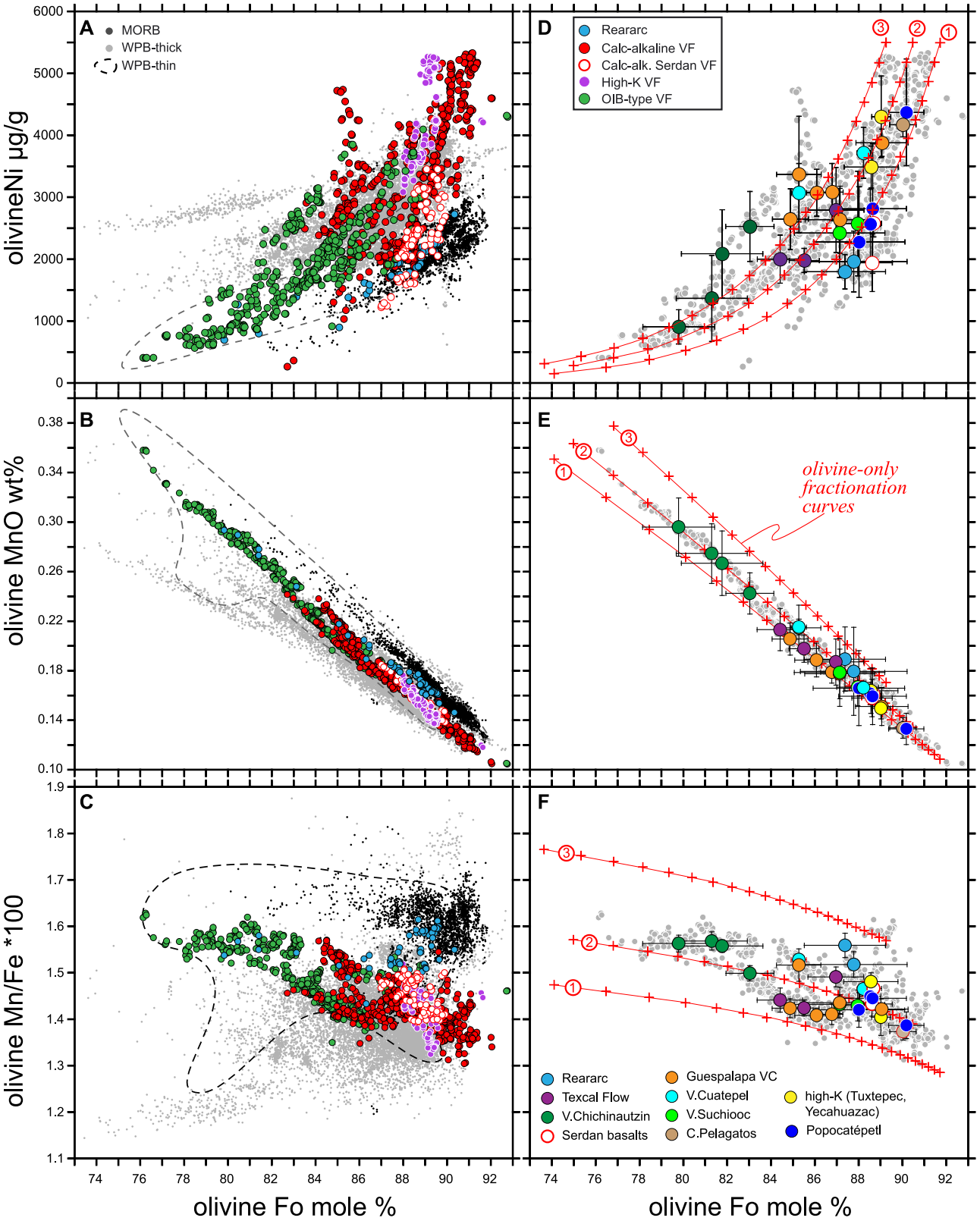

Fig. 2. (a–c) TMVB olivine Fo (mole %) vs MnO (wt %) and Mn/Fe compared to MORB and WPB olivines from Sobolev *et al.* (2007). Analytical errors are within symbol size. (d–f) Individual symbols (colored filled circles) denote the average olivine composition (±1 SD) of individual, non-co-genetic magmas that come from different (different color) or the same volcanoes (same color). Small gray-filled circles—all olivines. Lines with crosses—model curves for olivine-only fractionation. Crosses mark 1% fractionation steps. Curves were modeled with a starting composition of 11 wt % MgO and Ni = 530 µg/g, but variable FeO and MnO concentrations (Curve 1: 6 wt % FeO*/0.095 wt % MnO; Curve 2: 7/0.12; Curve 3: 8/0.155) with partitioning data from Beattie *et al.* (1993, 1991) for MnO, and from Hart & Davis (1978) for olivine Ni. Coloring and symbols are that same as in Straub *et al.* (2023), except for the high-K olivines that are now also distinguished.

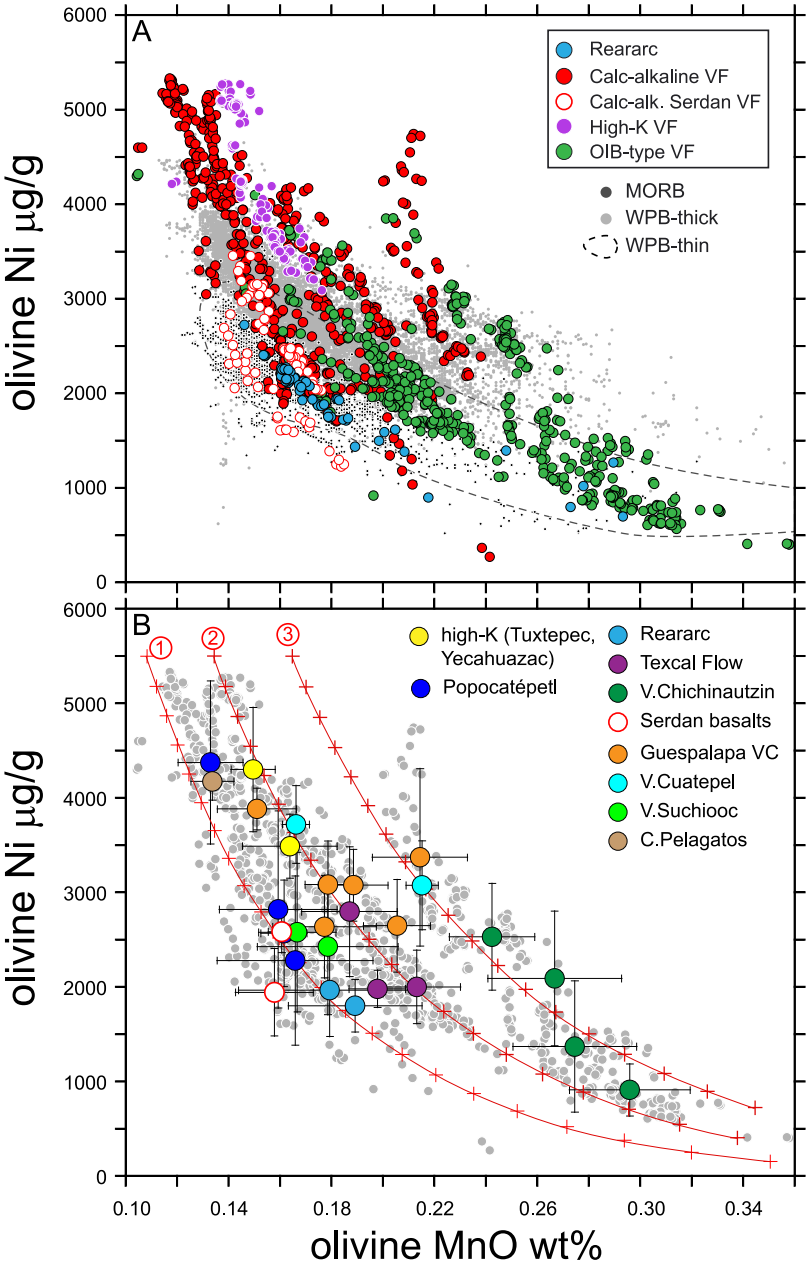

Fig. 3. Olivine MnO wt % vs Ni µg/g. Symbols as in Fig. 2.

T^{Al}_{oliv} of 909–992 °C are excluded, the range narrows to 1047–1244 °C with an average 1127 ± 39°C. There are several notable correlations: first, the T^{Al}_{oliv} vary systematically with location and compositional groups: the arc-front olivines crystallize at ~100 °C lower (T^{Al}_{oliv} = 1119 ± 38 °C) than the rear-arc olivines (= 1213 ± 18 °C). Additionally, the arc-front OIB-type olivines have slightly higher T^{Al}_{oliv} = 1147 ± 25 °C than the calc-alkaline/high-K olivines (T^{Al}_{oliv} = 1108 ± 37 °C), and the calc-alkaline Popocatépetl olivines have the lowest T^{Al}_{oliv} of 1088 ± 47 °C, even without the three outlying T^{Al}_{oliv}. Second, the average T^{Al}_{oliv} per sample correlates inversely with the TMVB bulk rock SiO_2 (48–60 wt %; $R^2 = 0.71$, $n = 34$), excepting the olivine antecrysts in the Popocatépetl dacites (Fig. 5c). Again, this trend cannot be generated by fractional crystallization because it includes four non-co-genetic magmas groups, whereby most individual samples within each magma group are not co-genetic (see above). Thirdly, with decreasing T^{Al}_{oliv}, the characteristic slab signature of incompatible trace elements gets stronger, the Cr-spinel Cr# [$R^2 = 0.61$, $n = 34$; see fig. 11 in Straub *et al.* (2023)] and the melt water concentrations overall increase. Melt water in the rear-arc magmas range between 0 and 2.3 wt % H_2O based on plagioclase hygrometry (Díaz-Bravo *et al.*, 2014), to up to ~1 wt % H_2O in OIB-type magma (Cervantes & Wallace, 2003*b*) and up to 5.2 wt % H_2O in calc-alkaline and high-K magmas (Cervantes & Wallace, 2003*a*; Roberge *et al.*, 2009) (all melt inclusion data in forsteritic olivine). Collectively, these observations show that the fertile rear-arc magmas (free from slab influence) have the highest olivine crystallization temperatures, whereas the lowest olivine crystallization temperatures are found in the silicic, hydrous calc-alkaline magmas that originate from depleted ambient arc front mantle (Straub *et al.*, 2014, 2015, 2023).

Regardless of the internal TMVB systematics, the TMVB arc front magmas have in their entirety lower T^{Al}_{oliv} than MORB olivines (average = 1265 ± 54 °C); WPB olivines (Iceland and Hawaii; = 1284 ± 33 °C) and the olivines from large-igneous provinces (LIP)

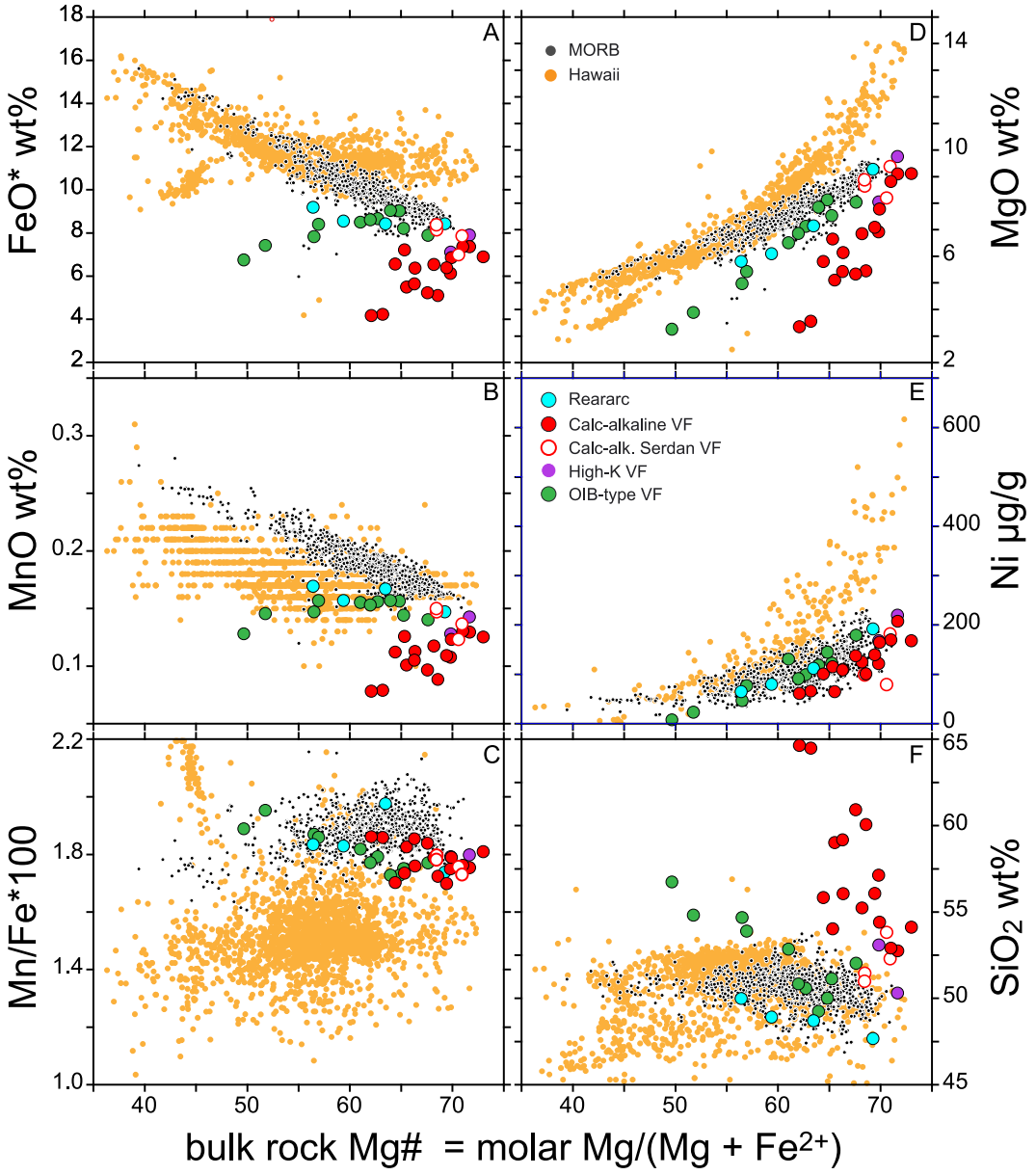

Fig. 4. (a–f) Major element oxides of volcanic rocks from the TMVB, mid-ocean ridges, and Hawaii (exemplifying WPB-thick). Hawaiian bulk rock data are from GeoROC. (2024) (downloaded on 2 October 2024), and—following Yu & Langmuir (2023)—filtered for compositions with all major element oxides, total sum of oxides between 99 and 101 wt %, and that are not classified as 'post-shield', 'pyroclastic', or 'moderately' and 'highly altered'. This yields 2372 samples, with Ni concentrations in 424 samples. Iron is calculated as total FeO∗ with FeO = Fe_2O_3/1.111. MORB data (glasses only) are from Jenner & O'Neill (2012) and Yang *et al.* (2018).

(= 1323 ± 89 °C). The TMVB rear-arc olivines, however, have higher T^{Al}_{oliv} that overlap with those of MORB and WPB olivines (Figs 4 and 6). Despite their limited T^{Al}_{oliv} range, the TMVB arc front olivines exhibit a similar large—and even larger—range in Fo and Ni, Cr-spinel Cr#, and olivine MnO than MORB and WPB olivines. Note that T^{Al}_{oliv} data from MORB and WPB are still relatively sparse, which compromises the comparison. For example, the high TMVB olivine Ni may not be as outlying as than shown, given that no T^{Al}_{oliv} are available for the high-Ni Hawaiian (~WPB-thick) olivines (see brown bar in Fig. 5b).

DISCUSSION

A central result of our study is the similar Fo-Ni-MnO systematics of TMVB arc front and Hawaiian (~WPB-thick) olivines despite TMVB and Hawaiian magmas have very different melt compositions, olivine crystallization temperatures and mantle melting conditions. Hawaiian primary melts are thought to form in garnet-bearing peridotite mantle, at pressures of up to ~4.5 GPa (~150–160 km depth) (Yu & Langmuir, 2023) and high $T_{sources}$ of ~1500 °C (Putirka, 2005; Herzberg *et al.*, 2007). Matzen *et al.* (2017) and Yu & Langmuir (2023) propose that the inverse array of forsteritic WBP olivines normalized to Fo_{89} in the olivine MnO vs Ni space (Fig. 7a) was caused by variation in the extent and depth of melting modulated by lithospheric thickness: low-Ni, high-MnO olivines reflected shallow melting beneath thinner lithosphere, while high-Ni, low-MnO olivines signaled deep, hot melting in the garnet-bearing mantle source beneath thick lithosphere. The TMVB olivines with Fo > 88 (high-Fo > 88 olivines) form a similar, overlapping inverse correlation, where the arc front olivines

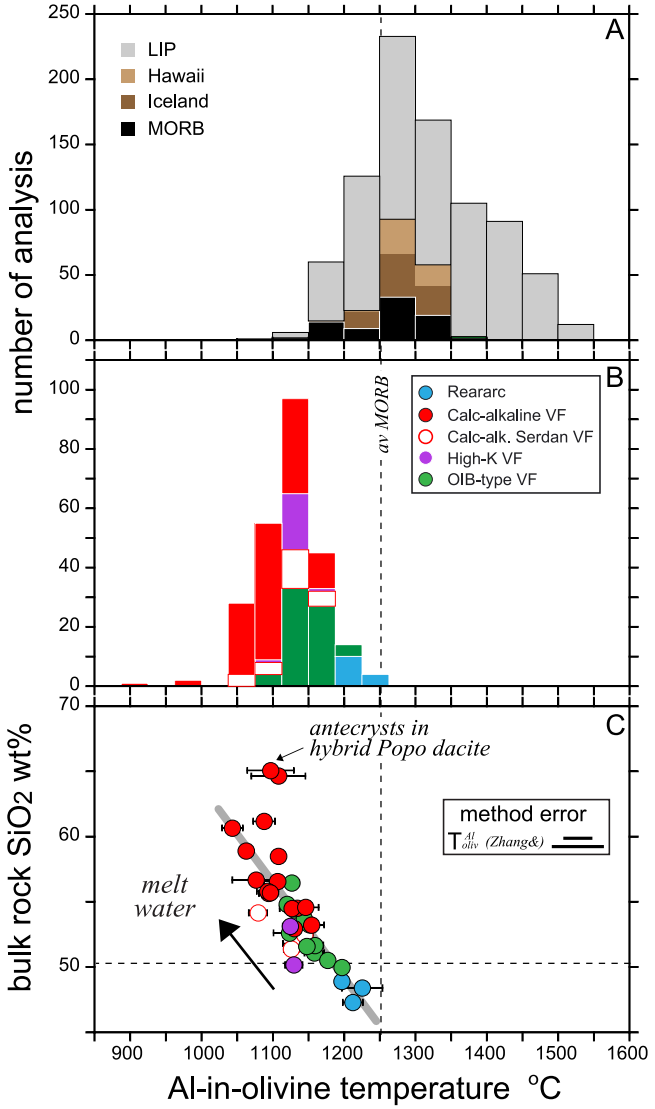

Fig. 5. Olivine crystallization temperatures (T^{Al}_{oliv}) from olivine–spinel aluminum exchange thermometry in degree Celsius (°C) calculated after Zhang *et al.* (2023) (method error of ±24 or ±43 °C) (Table S4) (a) MORB, WPB, and LIP. Data sources: MORB (Coogan *et al.*, 2014; Matthews *et al.*, 2021), including data from the Dragon Flag Supersegment: Li *et al.* (2021); WPB (Hawaii, Iceland): Matthews *et al.* (2016, 2021) and Spice *et al.* (2016); LIP: Spice *et al.* (2016), Xu & Liu (2016), Zhang *et al.* (2021), Wu *et al.* (2022); Coogan *et al.* (2014), Jennings *et al.* (2019), and Trela *et al.* (2017). (b) Histogram of T^{Al}_{oliv} for TMVB olivine-Cr-spinel pairs. (c) Average T^{Al}_{oliv} per sample vs bulk rock SiO_2 wt %, with a correlation coefficient $R^2 = 0.71$ for 34 samples (thick gray line), which excludes the olivine antecrysts in the hybrid Popocatépetl dacites. Error bars are 1 SD of the averaged T^{Al}_{oliv} per rock sample. Arrow denotes overall increase of meltwater concentrations (see text).

overlap with the WPB-thick olivines and extend their trend to higher Ni and lower MnO concentrations (Fig. 8a). However, the WPB genetic model cannot apply in the TMVB. First, most TMVB arc front magmas lack garnet signatures, except for the rare monogenetic high-K magmas (Straub *et al.*, 2015). The latter are outliers and not end-members of a trend (Fig. 7b) that would allow for suspecting residual garnet in the mantle source. Second, in the Popocatépetl/SCVF arc front segment, where high-Ni olivines are common, subduction geometry limits the pressures of mantle melting to somewhere between ≥ ~1.2 GPa (~45 km, Moho) and < ~2.4 GPa (~90 km, slab top) (Pardo & Suarez, 1995; Perez-Campos *et al.*, 2008). Given the inverted thermal structure of arc mantle wedges and the existence of a refractory lithosphere beneath the crust, the actual pressure range of melting is likely smaller and somewhere in the middle of the theoretical maximum range. Low melting pressures limit the potential for a large ΔT that can greatly increase the $Kd^{Ni}_{oliv/melt}$ and olivine Ni. Also, in the rear-arc and at Serdán, where the slab top is >200 km deep below the volcanoes, and the pressure and temperature range of melting could be much greater, high-Ni, low-MnO olivines are virtually absent.

How can the TMVB and Hawaii (~WPB-thick) produce similar olivine Fo-Ni-MnO systematics under such different melting conditions? Does this require different source lithologies in the TMVB, such as peridotite versus pyroxenite? Or do cooler, silicic melts of the TMVB modulate the olivine Fo-Ni-MnO systematics through the temperature- and composition-sensitive olivine/melt Kds? We proceed by testing quantitatively whether silicic, cooler, and hydrous primary melts of peridotite can reproduce the TMVB olivine Fo-Ni-MnO systematics.

Melting conditions beneath the central TMVB

The modeling of the olivine/melt partitioning requires the T_{source} (temperature of melt extraction) and the ΔT as input, which can be calculated with the Mitchell & Grove (2015) model for hydrous peridotite melting, using TMVB primary melts compositions and their H_2O concentrations. The Mitchell & Grove (2015) model is calibrated based on inverse thermobarometric experiments of primitive hydrous, high-Mg# arc basalts and andesites, which include rock samples from TMVB, and even one sample from the monogenetic Cerro Pelagatos, which is studied here for the olivines (Weaver *et al.*, 2011; Weber *et al.*, 2011) (Table S1). We also tested the silica activity models from Putirka (2008) and Lee *et al.* (2009). However, these models predict far too shallow melting pressures within the TMVB crustal basement. Next, we define the model input and discuss the results of the Mitchell & Grove (2015) model.

Identifying the composition of primary TMVB melts

To identify potential primary TMVB melts in our sample set, all 37 bulk rocks and their olivines were screened for those that have olivines with Fo >88, and where in addition the most forsteritic olivines are in equilibrium with the bulk rock. Eight of the 10 samples that pass this screen are within the calibration range of the Mitchell & Grove (2015) melting model with bulk rock Mg# = 69–73, MgO = 8.1–9.7 wt %, SiO_2 = 50.2–54.5 wt %, Cr = 264–621 μg/g, and Ni = 79–220 μg/g. (see Supplement B for more details of the screening, and Table S5 for composition). These eight samples (seven calc-alkaline/high-K basalts and basaltic andesites, one OIB-type basaltic andesite) match the primary arc melt criteria from Schmidt & Jagoutz (2017) and thus are considered to be primary TMVB melts. The eight samples have slightly variable melt Mg#, Ni, MgO, FeO, SiO_2, and H_2O concentrations, and often individual olivine Fo-Ni-MnO signatures. This is due to the inherent compositional variability of the primary TMVB melts that are sourced from a mantle wedge made heterogeneous by slab fluxing and variable melt extraction (Straub *et al.*, 2013, 2014; Ahmadi *et al.*, 2025).

Meltwater concentrations of primary TMVB melts

Meltwater concentrations for the eight primary melts were calculated with the Ni hygrometer of Pu *et al.* (2024) (method error ± 0.5 wt %) (Table S5). The Ni hygrometer is calibrated for basaltic to mafic andesitic melts that crystallize olivines

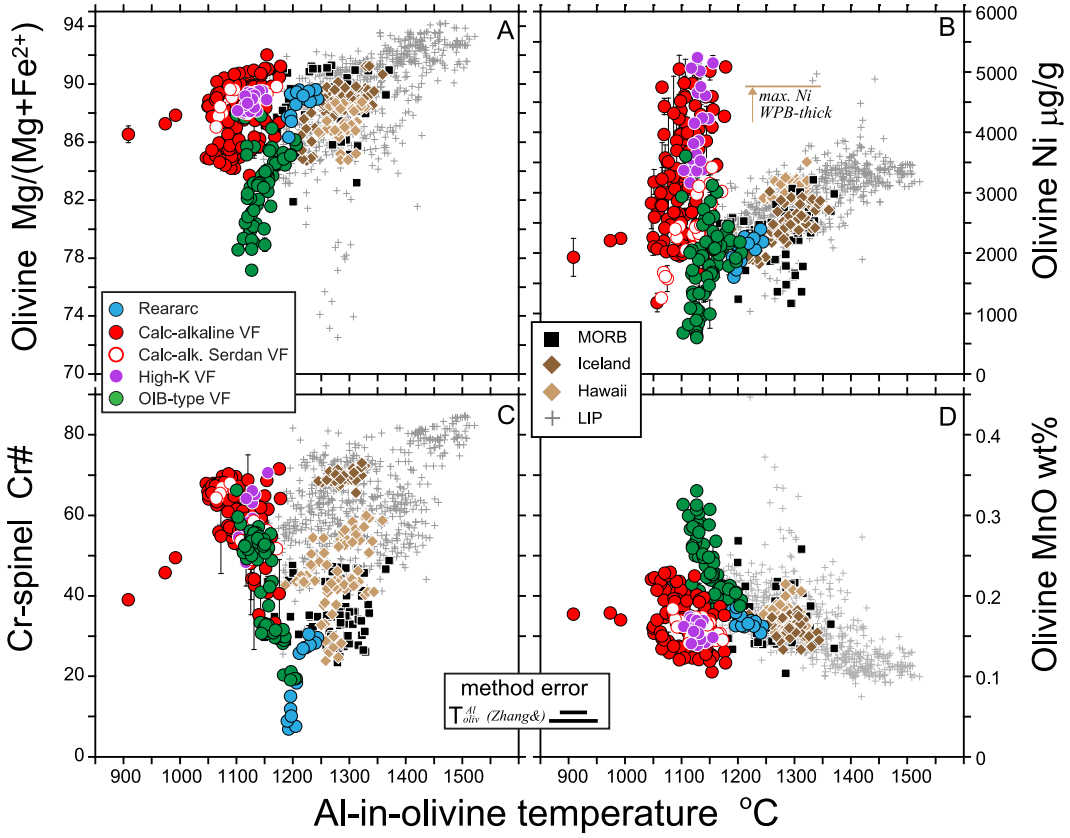

Fig. 6. Olivine crystallization temperatures (T^{Al}_{oliv}) in degree Celsius (°C) vs olivine Mg# (a), olivine Ni (µg/g) (b), Cr-spinel Cr# (c), and olivine MnO wt % (d). Error bars for TMVB olivines (which are often within symbol size) are ±1 SD of the average Fo, Cr#, Ni, and Mn calculated of all paired olivine–spinel of a single olivine crystal. Horizontal bar marked 'max. Ni WPB-thick' in panel B indicates the maximum Ni in the Hawaiian Koolau olivines (Sobolev *et al.*, 2007) for which no T^{Al}_{oliv} data exist. Data sources and other symbols as in Fig. 5. Method errors (±24 °C and ± 43 °C) are based on Zhang *et al.* (2023).

with $Fo_{78–95}$ at crustal pressures ≤1 GPa and melt temperatures between 1024 and 1220 °C, and it requires knowing the pressure of olivine crystallization. Experimental olivine+Cr-spinels can crystallize at pressure up to 1 GPa (~37 km depth) in hydrous high-MgO basalts (Blatter *et al.*, 2013; Ulmer *et al.*, 2018). However, crystallization pressures ≤1 GPa do not strongly influence the calculated meltwater of the Pu *et al.* (2024) hygrometer. For example, for pressures of 0 and 1 GPa, the hygrometer yields melt H_2O = 2.7–8.7 wt % (average 6.0 + 2.1 wt %), and H_2O = 4.1–10.1 wt % (average = 7.4 + 2.1 wt %), respectively. The averages are barely outside the method error. We calculated melt H_2O concentrations for an intermediate crystallization pressure of 0.4 GPa (~15 km depth), which is the currently known maximum crystallization depth obtained from H_2O-CO_2 barometric data of the TMVB olivine melt inclusions (Cervantes & Wallace, 2003*a*; Cervantes & Wallace, 2003*b*; Roberge *et al.*, 2009). The calculated melt H_2O ranges between 4.0 and 9.2 wt % at an average of 6.6 ± 2.2 wt % H_2O (Table S5). For any pressure between 0 and 1 GPa, the calculated melt H_2O is higher than measured in olivine melt inclusions (2.4–5.2 wt % H_2O; average 3.7 ± 1.2 wt % H_2O) (Cervantes & Wallace, 2003*a*; Roberge *et al.*, 2009). This is not unexpected, because melt inclusion H_2O data are often minimum values owing to crystallization-driven degassing and diffusive H_2O loss.

Olivine crystallization temperatures of primary TMVB melts

At a pressure of 0.4 GPa, the Pu *et al.* (2024) thermometer (method error ± 29 °C) yields olivine crystallization temperatures (T^{oliv}_{cryst}) of 1053–1161 °C (average 1103 ± 39 °C) for the eight primary melts. For the same pressure and melt H_2O, the olivine/melt thermometer (eq. 22) of Putirka (2008) (method error ± 29 °C; calibrated for basaltic to andesitic melts with 0–18.6 wt % H_2O and temperatures between ~1000 and 2000 °C) yields similar crystallization temperatures T^{oliv}_{cryst} = 1068–1158 °C (average 1108 ± 32 °C) (Table S5). The T^{oliv}_{cryst} are not sensitive to pressures: assuming crystallization pressures and corresponding meltwater content for pressures between 0 and 1 GPa, the discrepancy in T^{oliv}_{cryst} is not larger than ~20–29 °C and within the method errors of the Pu *et al.* (2024) and Putirka (2008) thermometers.

Gratifyingly, the T^{oliv}_{cryst} after Pu *et al.* (2024) and Putirka (2008) are comparable to the crystallization temperatures obtained for eight primary melts from OSAT thermometry (T^{Al}_{oliv} =1079–1154 °C, at an average T^{Al}_{oliv} =1128 ± 28 °C, whereby the T^{Al}_{oliv} per rock sample is calculated the average T^{Al}_{oliv} obtained from all individual olivine–Cr pairs; Table S5). The T^{oliv}_{cryst} and T^{Al}_{oliv} of the eight samples are not correlated (Fig. 8), which may reflect the error of treatment stemming from the olivine/melt equilibria. Interestingly, the T^{Al}_{oliv} are often slightly higher than the T^{oliv}_{cryst} (Fig. 9) (excepting the single OIB-type sample), which argues against the T^{Al}_{oliv} being lowered by post-crystallization subsolidus Fe–Mg exchange (Zhang *et al.*, 2023; Blatter & Burgess, 2025). Overall, given the independent methodologies, the overlap of T^{oliv}_{cryst} and T^{Al}_{oliv} confirm the low olivine crystallization temperatures of the high-Mg# arc front magmas.

Pressure and temperatures of mantle melting

Primary melt compositions and melt H_2O calculated at 0.4 GPa were used to obtain pressures and temperatures (~T_{source}) of melt extraction in the mantle with the Mitchell & Grove (2015) model

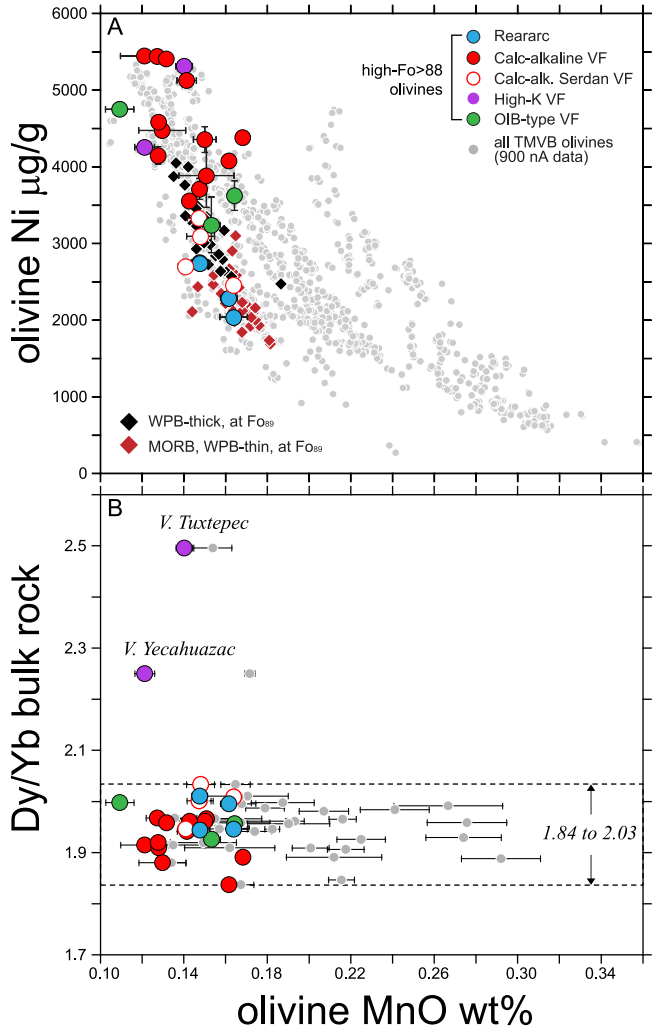

Fig. 7. (a) Olivine MnO wt % vs Ni µg/g for TMVB olivines compared to WPB-thick and WPB-thin olivines normalized to Fo_{89} from Matzen *et al.* (2017) (filled diamond symbols). (b) Olivine MnO of TMVB bulk rocks vs bulk rock Dy/Yb. Only 900 nA EMP data for TMVB olivines are shown for clarity. Large filled circles—all TMVB olivines with average 'high-Fo >88 olivines' (see Supplement B for olivine selection and definition). Error bars are ±1 SD of average Ni and MnO of the high-Fo >88 olivines. Small gray-filled circles all other TMVB olivines.

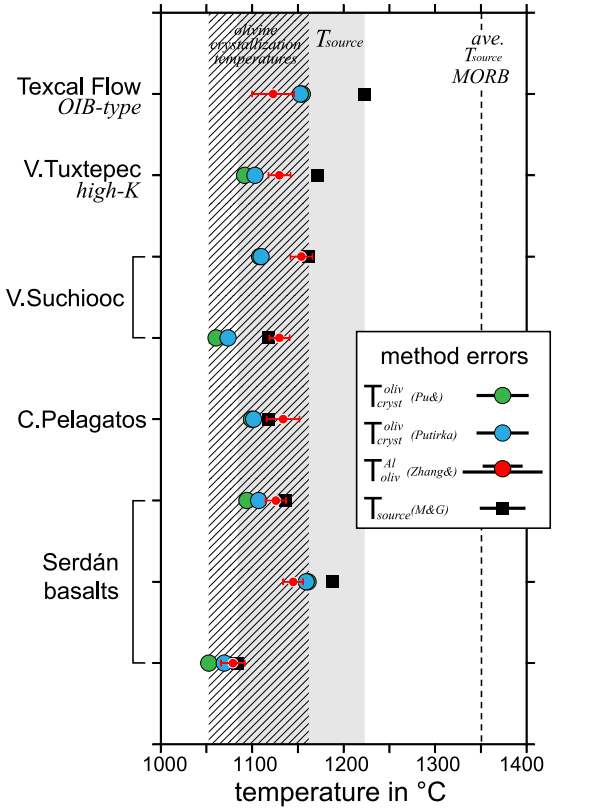

Fig. 8. Comparison of mantle source temperatures T_{source} and olivine crystallization temperatures calculated after Pu *et al.* (2024) (Pu&), Putirka (2008) (Putirka) and after Zhang *et al.* (2023) (Zhang&). T_{source} calculated after Mitchell & Grove (2015) (M&G). Bars on T^{Al}_{oliv} are ±1 SD of the average T^{Al}_{oliv} calculated from all individual olivine-Cr-spinel pairs per sample. Bars in legend denote method errors (see text). Hatched field—range of olivine crystallization temperatures. Shaded field—range of T_{source}. Samples are ordered by longitude (not to scale). Average MORB source temperature after Brown Krein *et al.* (2021).

(Fig. 9). This model is calibrated for mantle melting temperatures between 1100 and 1600 °C (method error ±25 °C) at pressures between 1 and 2.5 GPa (method error of ±0.14 GPa). For the eight TMVB primary melts, the mantle pressures range between 1.4 and 1.9 GPa (~51–69 km), averaging 1.6 ± 0.2 GPa (~58 ± 7 km). The mantle temperatures (~T_{source}) range from 1084 to 1223 °C, with an average of 1150 ± 45 °C (Fig. 8). Variations in melt H_2O, which depend on the chosen olivine crystallization pressures between 0 and 1 GPa, do not much affect these mantle pressures and temperatures. Overall, these low $T_{sources}$ are realistic for the hydrous peridotite mantle melting, where the mantle solidus is lower ~100–220 °C than the anhydrous solidus at the given H_2O concentrations (e.g. Tenner *et al.*, 2012; Till, 2017). There is also internal consistency in the TMVB data that supports the results. First, the highest T_{source} = 1223 °C is calculated for the least hydrous, OIB-type arc front melt. Second, the highest pressure, 1.9 GPa (~70 km, halfway between the Moho and the slab top), is obtained for the basaltic high-K melt (Tuxtepec) that exhibits a rare garnet signature (Fig. 8b).

Estimating ΔT in the TMVB

The ΔT was calculated as the difference between T_{source} and the three olivine/melt crystallization temperatures (T^{oliv}_{cryst} after Pu *et al.* (2024) and Putirka (2008); T^{Al}_{oliv} after Zhang *et al.* (2023)) (Table S5; Fig. 9). The ΔTs calculated with the T^{oliv}_{cryst}s are all positive, with averages of ΔT = 47 ± 21 °C [using T^{oliv}_{cryst} after Pu *et al.* (2024)] and ΔT = 42 ± 22 °C [using T^{oliv}_{cryst} after Putirka (2008)], respectively. This is expected because the melt compositions (including H_2O) are the same, while only the pressures (of melt extraction vs crystallization) are different. In contrast, the ΔTs calculated with T^{Al}_{oliv} (which are completely independent from the T_{source} calculation) are smaller and more variable (average ΔT = 23 ± 38 °C) and can be zero within the error of the methods (Fig. 9). The important information is that all ΔTs are zero or positive, which is consistent with the concept of some melt cooling during ascent, which may even be absent if the melts ascend too fast for measurable cooling (e.g. Blatter & Burgess, 2025).

We calculated an average ΔT for the individual samples by averaging all three ΔTs for more robustness (Table S5). These average ΔTs range from 7 to 80 °C, possibly due to variable extent of melt cooling at the individual volcanoes. For modeling purposes, we use the maximum ΔT of ~80 °C calculated for the OIB-type melt, and the maximum of ~64 °C for calc-alkaline/high-K melts, because this maximizes the temperature-driven increase of the $Kd^{Ni}_{oliv/melt}$.

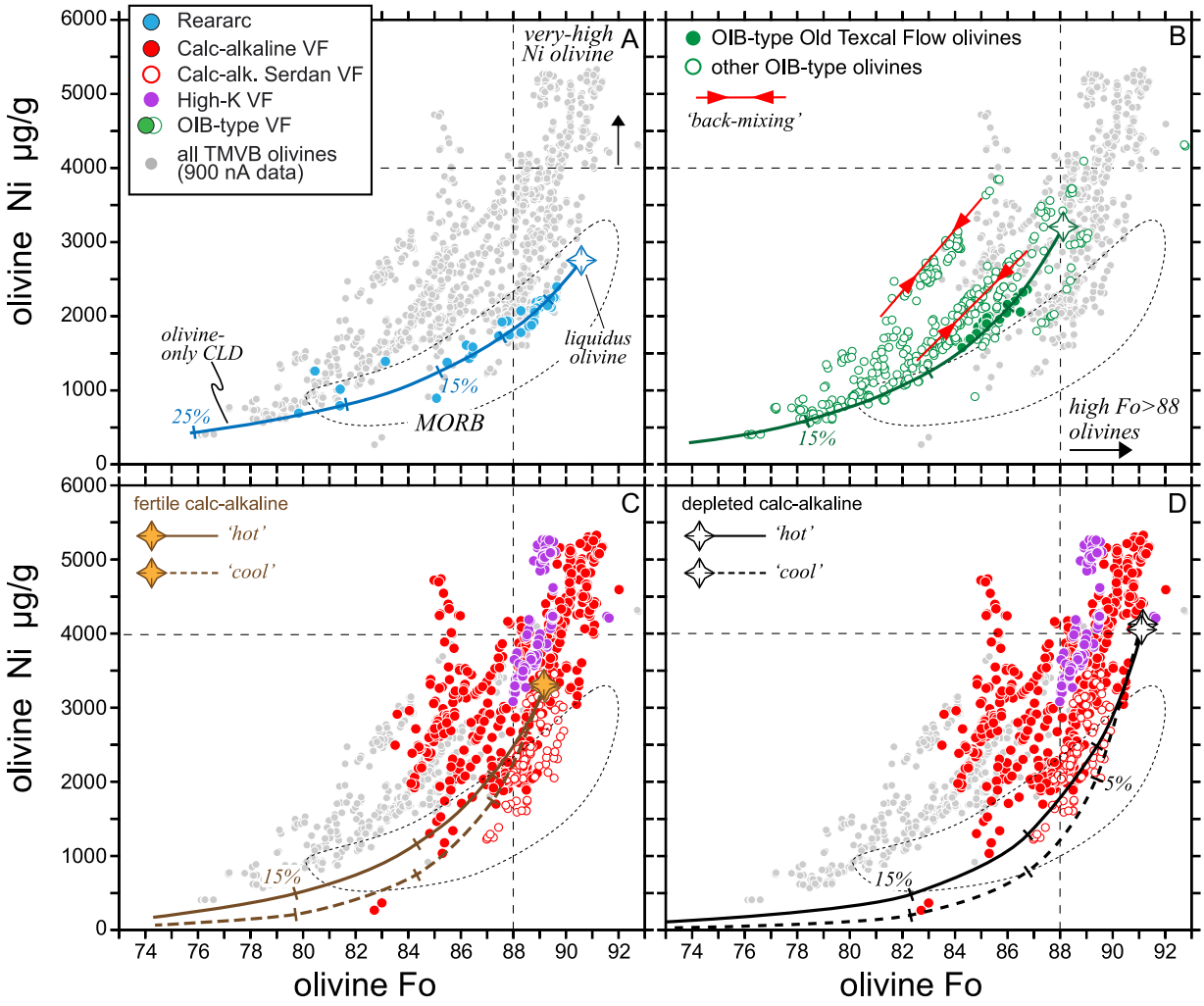

Fig. 9. Model results for olivine Fo vs Ni µg/g calculated with data in Table 1. Star symbols—olivines on the liquidus of mantle melts. Thick curved lines—crystal-lines-of-descent for olivine-only fractionation with tick marks indicating olivine loss in 5% steps. Stippled outline—Field of MORB olivines from Sobolev *et al.* (2007). Only 900 nA EMP data for TMVB olivines are shown for clarity. Vertical stippled lines separate olivines with Fo ≥88 (approximately in or near equilibrium with mantle melts) from olivines with Fo ≤88 that can be more strongly affected by crustal processing. Horizontal stippled lines in Fo-Ni space denote the estimated maximum olivine Ni concentration (~4000 µg/g) achievable in partial peridotite melts. (a) Rear-arc olivines, (b) OIB-type arc front olivines, with OIB-type Old Texcal Flow singled out (filled circles). Double arrow-labeled 'back-mixing'—typically straight melt mixing trajectories caused (by recharge) melt mixing in the crust (e.g. Straub *et al.*, 2013, 2014; Gleeson & Gibson, 2019). (c) Olivine in calc-alkaline/high-K melts from fertile 'hot' and 'cool' mantle. (d) Olivine in calc-alkaline/high-K melts from fertile 'hot' and 'cool' mantle. See text for definitions.

Modeling olivine in equilibrium with primary TMVB melts

The high-Ni olivines were previously modeled with the polybaric decompression melting model of Langmuir *et al.* (1992). This model predicts melt temperature, MgO, FeO∗, and Ni from the composition of mantle olivine for a given pressure of melting. However, the primary melts produced are too mafic (>10 wt % MgO) and too hot (>1400 °C) for the TMVB (Straub *et al.*, 2008, 2011*b*, 2013). There is no such forward melting model for the cooler, hydrous, and silicic arc magmas. Therefore, we defined four 'representative' primary melts to illustrate the influence of melt composition and temperature on the olivine Fo-Ni-MnO. These 'representative' primary melts are based on the observed primitive melt compositions and as close as possible to observed compositions. We chose one melt to represent the rear-arc, and three melts to represent the arc front: one OIB-type melt and two calc-alkaline/high-K melts for representing the end-member melts from the 'fertile' vs 'depleted' TMVB arc front mantle identified by Straub *et al.* (2011*b*).

Rear-arc melt

The representative rear-arc melt illustrates the olivine Fo-Ni-MnO variability in a basaltic mantle melts free from slab influence. Melt SiO_2 = 49 wt %, FeO∗ = 8 wt %, and MnO = 0.155 wt % are chosen to match the rear-arc basalts with the highest bulk rock Mg# (Fig. 4). Melt MgO was increased to 13 wt % to achieve equilibrium with the highest olivine $Fo_{90.6}$ observed; this results in a bulk rock Mg# ~74 and corresponds to ~15% olivine-only addition to the observed melt. Given the olivine loss, the observed maximum Ni = 191 µg/g of the rear-arc basalts is too low. For example, we assume a low ~2400 µg/g Ni in the olivine of the mantle source [the 95% confidence interval for mantle Ni in the TMVB ranges from ~2200 to 3400 µg/g Ni based on peridotite xenoliths from within and behind the TMVB (Heinrich & Besch, 1992, Nimz *et al.*, 1995, Luhr & Gomez-Aranda, 1997, Blatter & Carmichael, 1998)]. Using the calculation of Matzen *et al.* (2017) with the $Kd^{Ni}_{oliv/melt}$ from Yu & Langmuir (2023), and the primary melts has Ni = 332 µg/g for a MORB-type source temperature T_{source} of 1350 °C (e.g. Brown Krein *et al.*, 2021).

Arc front melts

To facilitate comparison, all three representative arc front melts are assumed to have 10 wt % MgO, which is close to the maximum bulk rock MgO = 9.7 wt % observed in the primary melts. The representative OIB-type melt was modeled with the typical SiO_2 = 50 wt %, high FeO* = 8.0 wt %, and MnO = 0.143 wt % for high-Mg# OIB-type melts (Fig. 4), which are in equilibrium with Fo_{88} olivines (Straub *et al.*, 2013). Two representative calc-alkaline/high-K melts from 'fertile' and 'depleted' arc front mantle source, respectively, were used to illustrate the influence of mantle fertility on the olivine Fo-Ni-MnO variations. The fertile melt has FeO* = 7.2 wt % and is in equilibrium with $Fo_{89.2}$ olivine at a bulk rock Mg# = 71.2; the depleted melt has FeO* = 5.8 wt % and is in equilibrium with $Fo_{91.1}$ olivine at a bulk rock Mg# = 75.4. Such a range of olivine Fo_{89} to Fo_{91} in mantle melts can be due to inherent mantle heterogeneity. However, it can also reflect melt origin from a mantle that has been made heterogeneous by variable degrees of slab flux-driven melt extraction until the clinopyroxene-out (Straub *et al.*, 2008, 2011*b*). The calc-alkaline/high-K melts were allotted the highest observed melt SiO_2 ~55 wt % (to maximize $Kd^{Ni}_{oliv/melt}$), and a bulk melt MnO of 0.13 wt % (fertile) and 0.10 wt % (depleted) melt, respectively, that match the range in the high-Mg# TMVB bulk rocks (Fig. 4).

The primary OIB-type magma has bulk rock Ni = 180 μg/g; the primary calc-alkaline/high-K melts have bulk rock Nis between ~80 and 220 μg/g (Table S5). Bulk rock Ni can be compromised by olivine fractionation, but it is important to note that a higher melt Ni is not expected for the TMVB arc front magmas. This is because the $Kd^{Ni}_{oliv/melt}$ increases (and with it the retention of Ni in the peridotite mantle), the cooler and the more polymerized (= more silicic, less magnesian) the primary mantle melts (Straub *et al.*, 2008). For example, assuming Ni = 2800 μg/g in the TMVB mantle olivines, a primary peridotite melt with 10 wt % MgO and 50 wt % SiO_2 and at a T_{source} of 1220 °C, had Ni ~234 μg/g. This is ~100 μg/g Ni less than in the rear-arc melt (= 332 μg/g Ni), despite the mantle olivine being more Ni-rich by 400 μg/g (Table 1). The effect is stronger for the primary calc-alkaline/high-K melts that are produced in even cooler mantle sources. We assume a slightly higher ~2900 μg/g Ni in mantle olivine of the fertile calc-alkaline/high-K primary melts [which corresponds to the mantle olivine Ni used by Matzen *et al.*, 2013 in their study of WPB olivines] at a still higher melt of 55 wt % SiO_2 at the same 10 wt % MgO. For the cool $T_{sources}$ of 1200 and 1100 °C, the Ni contents in the primary melts are only ~215 and 174 μg/g, respectively. For the depleted calc-alkaline/high-K primary melts, we use a high 3500 μg/g Ni in mantle olivine, which can be expected in a nearly harzburgitic mantle near the clinopyroxene-out. For the same melt composition, and $T_{sources}$ of 1200 and 1100°C, the melt Ni of ~260 and 210 μg/g, respectively, is only higher by ~55 μg/g, and still below the melt Ni of ≥300 μg/g expected for melt from MORB-type peridotite mantle (Langmuir *et al.*, 1992). Thus, it seems that the measured bulk rock Nis fairly well represent the actual melt Ni (Fig. 4).

With the primary melt compositions established, all other parameters can be calculated: primary melt Mg#, olivine MgO, FeO, Fo, MnO, Mn/Fe, and Ni of the liquidus olivine (with a $KD^{Fe/Mg}_{oliv/melt}$ = 0.30), as well as the $Kd^{Mg}_{oliv/melt}$, $Kd^{Fe}_{oliv/melt}$, $Kd^{Mn}_{oliv/melt}$, olivine Ni, MnO, and Mn/Fe. We tested the various Kds obtained with the equations of Beattie *et al.* (1991), Matzen *et al.* (2017), and Yu & Langmuir (2023) (Supplement C) and found them to yield very similar (but not identical) results. Here we used the Kds of Yu & Langmuir (2023), simply because their equation for the $Kd^{Ni}_{oliv/melt}$ includes a dependency on melt SiO_2. The Kds from Matzen *et al.* (2017) produce similar results within the error of the models. Primary melt compositions and selected calculated variables are summarized in Table 1 and displayed in various figures. The crystal-lines-of-descent for olivine-only fractionation are added to all figures to illustrate how olivine fractionation would influence olivine composition without implying that olivine fractionation caused these trends (see Figs 2 and 3).

Modeling results: olivine Fo-Ni variability

Rear-arc and OIB-type arc front magmas

The models for rear-arc and OIB-type olivines are compared in Fig. 9a and b. The olivines of the OIB-type 'Old Texcal Flow' are singled out (dark green-filled symbols), because the Old Texcal Flow most closely resembles a primitive melt from the fertile ambient mantle (= mantle without slab component) with only negligible slab additions (e.g. Ahmadi *et al.*, 2025, Straub *et al.*, 2013. The notable result is that Ni is higher in the Old Texcal Flow olivines (~3213 μg/g) than in the rear-arc olivine (~2775 μg/g), despite the rear-arc melt having higher Ni =332 μg/g than the OIB-type melt (= 234 μg/g Ni). This is because the $Kd^{Ni}_{oliv/melt}$ ~13.7 is higher in the OIB-type magmas than in the rear-arc magmas ($Kd^{Ni}_{oliv/melt}$ ~8.4), owing to lower melt MgO = 10 wt % and cooler T_{source} = 1220 °C (the rear-arc melt has MgO = 13 wt % and a T_{source} = 1350 °C). Because ΔT = 80 °C is the same in the two models, melt cooling has no net effect on the olivine Ni.

Most of the other OIB-type olivines (green open circles) have higher Ni than modeled in Fig. 9b. Possibly, these olivines crystallize in even cooler, more polymerized, and/or more Ni-rich melts. It is also possible that olivine Ni at lower <Fo_{88} is increased to some extent by complex crustal melt processing, including multiple recharge melt mixing before eruption (Straub *et al.*, 2008, 2013; Gleeson & Gibson, 2019). A detailed study of olivine zonation patterns may help to distinguish between these processes.

Calc-alkaline/high-K arc front magmas

Models for calc-alkaline/high-K olivines are shown in Fig. 9 for olivines in melts from fertile mantle (Fig. 9c) and depleted mantle (Fig. 9d), and for the two $T_{sources}$ of 1200 °C ('hot') and 1100 °C ('cool'), respectively. There are two notable results: first, while the melt Nis are comparatively low (175–260 μg/g), olivine Nis of high $Fo_{89–91}$ olivines are above the MORB olivine field with Ni ranging between 3270 and 3340 μg/g ('fertile') and 4071–4145 μg/g ('depleted'). Because melt Ni is so low, olivine Ni drops quickly by only moderate olivine fractionation, especially in the 'cooler' melt. Second, while the olivine Ni increases, the models do not reproduce the small population (~10%), TMVB olivine of very high-Ni olivines with ~>4150 μg/g. This failure is notable because the models were maxed out to achieve the highest Kd^{Ni}_{oliv} and olivine Ni. The ΔT of 64 °C is at its maximum and is in all likelihood even smaller, which would lower olivine Ni [Note that even doubling the ΔT to 128 °C is insufficient to reproduce the very high-Ni olivines]. The melt SiO_2 = 55 wt % and melt MgO = 10 wt % are those observed in the eight primary melts (Table S5). The 'cool' T_{source} of 1100 °C of the model cannot be further lowered because it is already below (by 20–70 °C) the T_{source} = 1118–1172 °C calculated by Mitchell & Grove (2015) model. This leaves an increase in melt Ni as only option to further increase olivine Ni. While an increase of ~50–60 μg/g Ni in the melt would reproduce the highest Ni calc-alkaline/high-K olivine, this 25% increase of melt Ni is not within the uncertainty of the models. The much simpler solution would be to increase melt Ni through melt–rock reaction in the mantle. While the modeling points to excess Ni

Table 1: 'Representative primary' melts used in modeling

	Rear-arc	OIB-type	Calc-alkaline/high-K			
			Fertile mantle		Depleted mantle	
			High T_{source}	Low T_{source}	High T_{source}	Low T_{source}
Melt SiO_2 wt %	49	50	55	55	55	55
Melt MgO wt %	13	10	10	10	10	10
Melt FeO wt %	8.0	8	7.20	7.20	5.8	5.8
T_{Source} °C	1350	1220	1200	1100	1200	1100
Mantle olivine Ni μg/g	2400	2800	2900	2900	3500	3500
ΔT °C	80	80	64	64	64	64
Melt Mg#	*74.3*	*69.0*	*71.2*	*71.2*	*75.4*	*75.4*
Olivine Fo mole %	*90.6*	*88.1*	*89.2*	*89.2*	*91.1*	*91.1*
Melt Ni μg/g	332	234	215	175	260	210
$Kd^{Ni}_{oliv/melt}$ *(source)*	*7.3*	*11.7*	*13.4*	*16.5*	*13.7*	*17.0*
$Kd^{Ni}_{oliv/melt}$ *(magma)*	*8.4*	*13.7*	*15.2*	*19.2*	*15.6*	*19.7*
Olivine Ni μg/g (magma)	*2775*	*3213*	*3274*	*3340*	*4071*	*4145*
Olivine Ni μg/g (source)	*2421*	*2733*	*2870*	*2869*	*3569*	*3560*
ΔT olivine Ni increase μg/g	*396*	*478*	*404*	*471*	*502*	*585*
Melt MnO wt %	0.155	0.143	0.13	0.13	0.10	0.10
$Kd^{Mn}_{oliv/melt}$	*0.92*	*1.13*	*1.15*	*1.15*	*1.20*	*1.20*
Olivine Mn μg/g (magma)	*0.143*	*0.161*	*0.15*	*0.15*	*0.12*	*0.12*

Regular font—input variables; italic font—variables calculated with the input variables. Calculated olivine data are for liquidus olivine only. Olivine/melt partition coefficients are calculated with equation from Yu & Langmuir (2023). Melt FeO is given as ferrous iron, owing to the small variations of the oxidation state [$Fe^{3+}/\Sigma Fe$ of 0.87 for TMVB from Straub *et al.* (2023)] relative to the large range of melt FeO*.

in the melts, additional support for such origin comes from the olivines in samples that contain very high-Ni olivines.

The very high-Ni olivines and their implication for mantle melts

In Fig. 10, very high-Ni olivines with Fo >88 from five samples are highlighted. Three of these samples belong to the eight primary melts listed in Table S5: the high-K monogenetic basalt (Tuxtepec) and two basaltic andesites from the monogenetic Suchiooc Cone. The other two samples are dacite lavas of the young Popocatépetl summit cone that contain olivine antecrysts that are likely residuals of mafic component melts injected into the Popocatépetl plumbing system (e.g. Straub & Martin-Del Pozzo, 2001). The olivines in these five samples form strikingly steep, subparallel trends in Fo–Ni space, with a very large range in olivine Ni (~5500–2000 μg/g) relative to Fo. The upper part of these trends (Ni ~>2500 μg/g) is too steep for olivine-only fractional crystallization (Fig. 11a). The zoning patterns of the olivines indeed show that the steep trends formed by magma mixing: at widely varying Ni concentrations in the olivine cores, the high-Ni olivine cores have normally zoned rims, and the low-Ni olivine cores have inversely zoned rims (Fig. 11). The olivine cores indicate the coexistence of high-Mg# melts in a plumbing system that must have different Ni concentrations or different degrees of polymerization or different melt temperatures, which enables them to crystallize olivines with similar Fo, but different Ni concentrations. The olivine rim zoning records the incomplete mixing of these magmas that typically occurs during ascent and eruption, where the magmas mingle before freezing (e.g. Bouvet de Maisonneuve *et al.*, 2016; Gordeychik *et al.*, 2018).

Which plumbing system contains magmas olivines with similar and high Fo >88 but different Ni in so close spatial and temporal proximity that these magmas incompletely mix before freezing? In such a system, the melt Mg# must be buffered (to produce olivines with similar Fo), while melt Ni and/or the $Kd^{Ni}_{oliv/melt}$ vary owing to variations in melt composition and temperature. We propose that such conditions can exist in mantle conduits (or network of conduits) where silicic slab components (hydrous melts, fluids, or diapirs) ascend through the ambient peridotite mantle and variably react with it. We visualize an open system that is sustained by the continuous addition of slab components that ascend to different mantle depths, and variably interact with the peridotite before eruption. In Fig. 12, several possible stages of such interaction are displayed. The construction of such a conduit may start with the absorption of silicic slab fluids into fertile peridotite mantle (dark green), which triggers partial melting and initial peridotite melt ascent (lighter green) (Fig. 12a). The melting leaves behind a partially depleted wall rock (lighter green) that continues to interact or react with new silicic slab components in various ways. For example, the reactive absorption of the silicic flux into the wall rock could form a lining of more fusible pyroxenite by transforming mantle olivine into secondary orthopyroxene (Fig. 12c). Upon melting, the fusible secondary pyroxenite then produces Ni-rich component melts. A percolating silicic melt may also absorb Ni by diffusion from the Ni-rich wall rock as proposed by Wang & Gaetani (2008). The silicic melt would also gain Fe, Mg (at the Mg# of mantle) from the wall rock, and be able to crystallize high-Fo, high-Ni olivines owing to a high $Kd^{Ni}_{oliv/melt}$ (Fig. 12d) (Wang & Gaetani, 2008). A combination of these processes is also possible: e.g. the diffusive exchange may happen with a peridotite wall rock that is already depleted by previous melting (Fig. 12e), or transformed to secondary pyroxenite (Fig. 12f).

Regardless of the details of the melt–rock interaction, the conduit (system) may contain melts with similar high Mg#, but different melt Ni, SiO_2, and MgO, as well as varying temperatures depending on the extent of melt–rock reaction and mantle depth. The melt–rock reaction processes may be most advanced in the

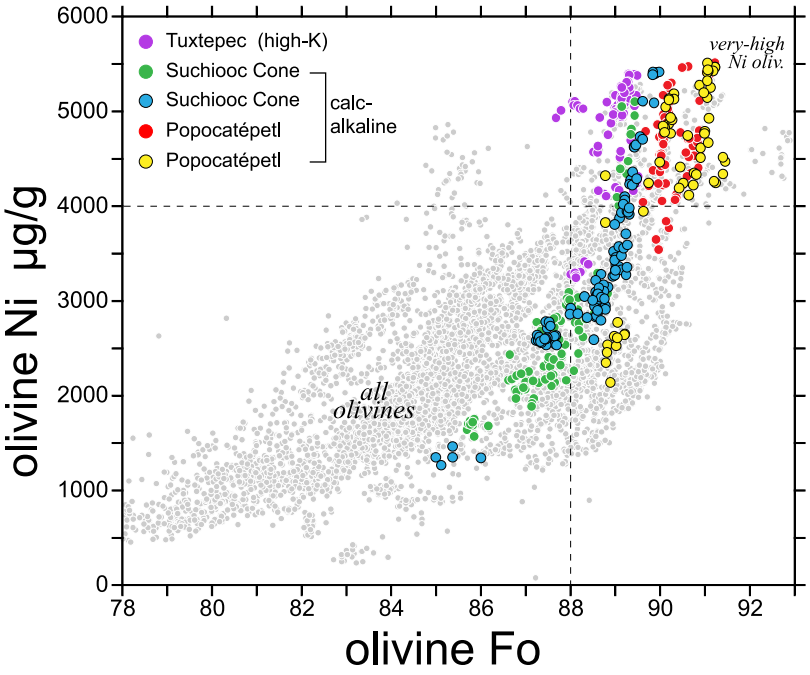

Fig. 10. Olivine Fo vs Ni µg/g for all data obtained with 100 and 900 nA beam currents. Five samples with very high-Ni olivines at Fo >88 are highlighted. One high-K basalt from monogenetic Tuxtepec (S15), two calc-alkaline basalts from monogenetic Suchiooc Cone (CH08–8, CH08–6); and olivine antecrysts from two Popocatépetl dacites (POS-2, POS-3). Stippled horizontal line at ~4000 µg/g Ni shows an approximate maximum in olivines from peridotite partial melts. Stippled vertical line—separated high-Fo >88 olivines.

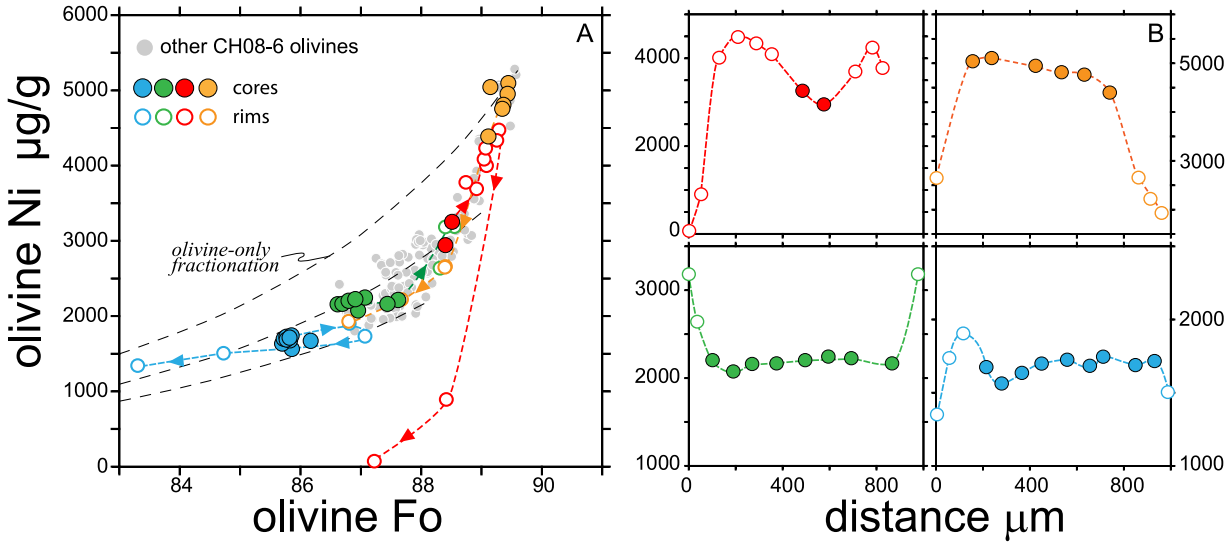

Fig. 11. (a) Olivine Fo vs Ni µg/g for calc-alkaline Suchiooc basalt CH-08-06 that has primary melt characteristics (SiO_2 = 53.2 wt %, MgO = 9.2 wt %, Mg# = 72 and Ni = 207 ppm). Individual olivines are highlighted by different colors. Filled colored circles—olivine cores; open colored circles—olivine rims, connected to cores by colored stippled lines. Black stippled lines—olivine-only crystal-lines-of-descent. (b) Core-rim profiles for selected olivine in panel (a) show normal and inverse zoning.

deeper parts that are most reachable by the slab flux, while peridotite partial melts may form more frequently at higher levels, which are more easily reached by the mobile, less viscous slab fluids. An important point is that such reacted melts must first ascend to levels of olivine saturation, which likely occur in the mid- to upper crust, before they mingle with other magmas containing low-Ni olivine, because otherwise the existence of these melts is not recorded. A simple model to explain the data would be the ascent of Ni-rich silicic melts to mid- to upper crustal levels, followed by crystallization of very high-Ni olivines just before mixing with residing magmas containing lower Ni olivines and final ascent and eruption.

Obviously, the survival of mantle melts capable of crystallizing very high-Ni olivines depends on their unimpeded ascent to levels of olivine saturation, rapidly followed by mixing and eruption before diffusive reequilibration can wipe out the signature. Such timescales are possible, as discussed by Ruprecht & Plank (2013) who showed that Ni-rich olivines in hybrid basaltic andesites of Irazú Volcano (Costa Rica) can ascend to the surface within months to days. In the Popocatépetl/SCVF segment, where high-Ni olivines are common, the combination of a high slab flux, a short mantle column, and an extensional crustal basement may promote the survival of Ni-rich mantle melts in monogenetic and composite volcanoes. On the other hand, it is entirely

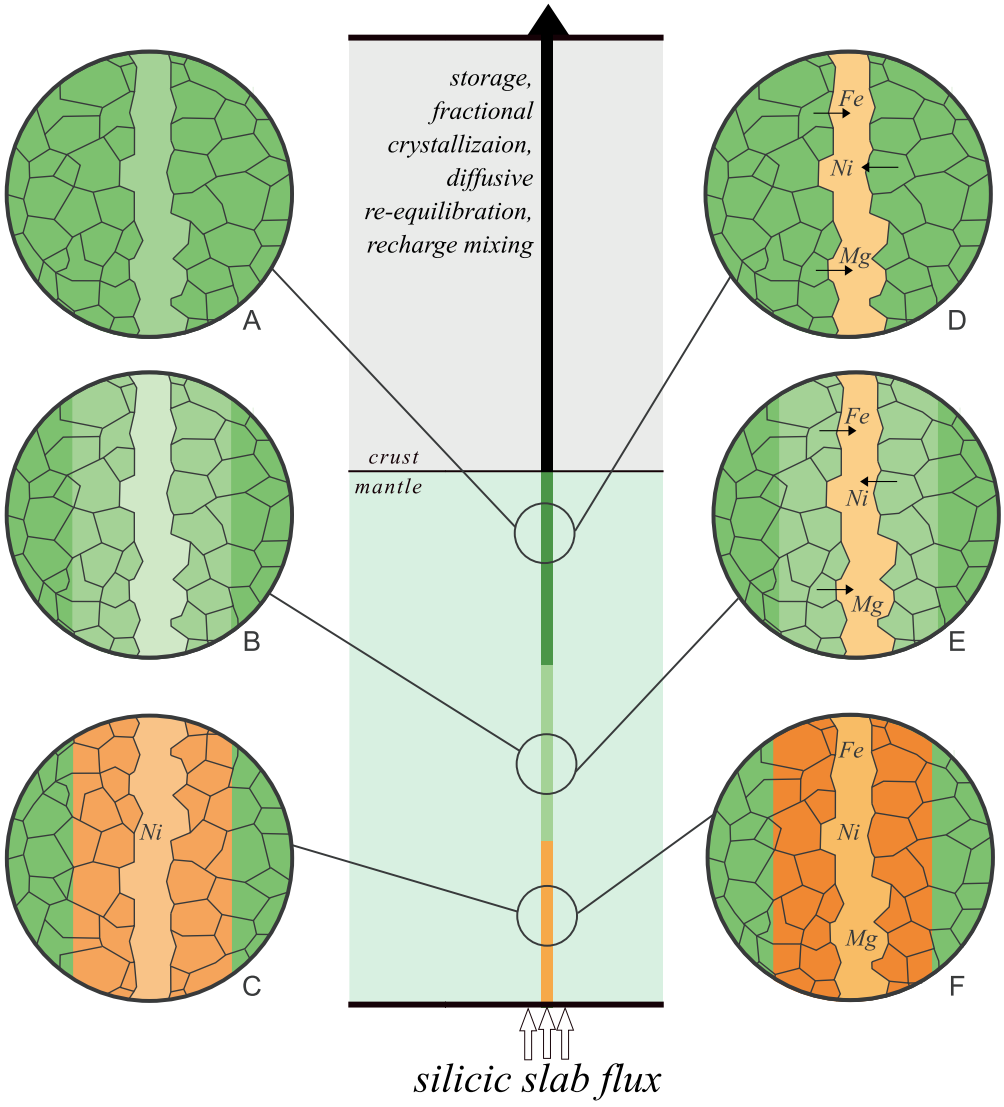

Fig. 12. Cartoon illustrating different stages of melt–rock interaction in a mantle conduit cutting through peridotite wall rock. Central panel: Idealized mantle conduit (system) that progressively changes as more silicic slab components infiltrate from below. Lower levels (most reachable from slab) are farther affected then more remote upper levels. Panels (a–f): Various stages of melt formation, mantle depletion and melt rock interaction discussed in text. (a) Initial partial peridotite melting; (b) Partial peridotite melt extracted from mantle partially depleted by previous melt extraction (lighter wall rock); (c) Ni-rich partial melt from wall rock that had been transformed to secondary pyroxenite by melt–rock reaction; (d) Hybrid silicic melt enriched in Fe, Ni, and Mg by diffusion exchange with wall rock; (e) Hybrid silicic melt enriched in Fe, Ni, and Mg by diffusion exchange with wall rock depleted by previous melt extraction; (f) Silicic melt percolating through conduit where wall rock was transformed to secondary pyroxenite, and enhanced by diffusive exchange. See text for more details.

perceivable that the Ni-rich mantle melts mix with other, low-Ni melts before olivine crystallization. Such hybridized melts would crystallize later olivines with lower Ni content and effectively conceal the existence of Ni-rich melts. This precarity might explain why very high-Ni olivine is rarely found in other volcanic arcs, simply because the Ni-rich mantle melts do not survive the ascent through the transcrustal volcano–magma system.

Modeling results: olivine Fo-MnO-Mn/Fe variability

The tight trends of olivine in Fo-MnO space contrast strikingly with their large range in olivine Ni olivines. This contrast reflects the different olivine/melt partitioning behavior for Ni and MnO: while the uptake of the highly compatible Ni is sensitive to melt temperature and composition, the mildly incompatible MnO is not sensitive to temperature and is only moderately affected by melt composition. Moreover, the olivine/melt exchange coefficients for MnO, FeO, and MgO are approximately constant ($KD^{Fe/Mg}_{oliv/melt}$ ~0.30; $KD^{Mn/Fe}_{oliv/melt}$ ~0.8) (Beattie *et al.*, 1991; Matzen *et al.*, 2017; Yu & Langmuir, 2023). This means that the magmatic olivines capture the MgO-FeO*-MnO signature of a (peridotite) mantle melt. Thus, the conspicuous displacement of arc front olivine Fo-MnO-Mn/Fe array relative to the MORB/rear-arc olivine array implies either that (1) the mantle source beneath the TMVB arc front is inherently different from the mantle of the MORB/rear-arc olivines, or that (2) there is some subduction-related mantle processing that collectively changes the melt MgO-FeO*-MnO systematics beneath the arc front. The latter possibility seems attractive, given that the rear-arc olivines resemble MORB olivines. Possibly, mechanisms include the formation of secondary mantle pyroxenites (Sobolev *et al.*, 2007), or the existence of residual accessory phases like garnet (Matzen *et al.*, 2017) or

phlogopite (Veter *et al.*, 2017). However, there is no evidence for the pervasive occurrence of such mantle phases in the TMVB mantle wedge that would affect the entire olivine Fo-MnO-Mn/Fe array.

First, and as discussed above, there is no evidence of widespread residual garnet in the TMVB arc front sources (Fig. 8), and the olivines in the rare high-K melts, which have garnet signatures, are inconspicuous in their olivine Fo-MnO-Mn/Fe characteristics. Second, the calc-alkaline/high-K and OIB-type arc front magmas give no evidence for residual phlogopite in source, which is present in the compositionally distinct, K-rich, phlogopite-bearing minettes, absarokites, and lamprophyres of western Mexico (Gómez-Tuena *et al.*, 2018). Thirdly, the results of this study indicate that many of the arc front olivines crystallize in hydrous peridotite melts, and thus do not need secondary pyroxenites in the source, which may shift the olivine Fo-MnO-Mn/Fe arrays (Sobolev *et al.*, 2007).

There is also the problem of whether secondary mantle pyroxenites can modify the olivine Fo-MnO-Mn/Fe systematics. While MnO is retained in mantle pyroxenites ($Kd^{Mn}_{opx/melt}$ ~0.352) relative to peridotite (the $Kd^{Mn}_{oliv/melt}$ ~0.259) (Beattie *et al.*, 1991, 1993), the Mn Kds are also linearly dependent on $Kd^{Mg}_{oliv/melt}$ and the $Kd^{Mg}_{opx/melt}$ (see equations in Supplement C). Because the $Kd^{Mg}_{opx/melt}$ is lower than the $Kd^{Mg}_{oliv/melt}$ (Beattie *et al.*, 1991, 1993; Yu & Langmuir, 2023), the MnO is also more easily released during melting, which cancels out (or even reverses) the effect of MnO retention. Theoretically, the olivine Fo-MnO arc front array may also shift by lowering Fo in the magmatic olivines. Olivines in melts from secondary pyroxenites have slightly lower Fo than melts from the original peridotite, because the $KD^{Fe/Mg}_{opx/melt}$ is lower than the olivine $KD^{Fe/Mg}_{oliv/melt}$ (Beattie *et al.*, 1991, 1993; Straub *et al.*, 2011*b*). However, for visibly displacing the TMVB Fo-MnO array, the lower $KD^{Fe/Mg}_{opx/melt}$ ~0.26 of Beattie *et al.* (1993, 1991) needs to apply, and not the higher $KD^{Fe/Mg}_{opx/melt} = 0.29 \pm 0.06$ inferred by Putirka (2008).

In view of these considerations, a distinct TMVB arc front ambient mantle seems a better solution. The TMVB olivine Fo-MnO-Mn/Fe array lies entirely within the range of WPB olivines (Fig. 2b and c), which represent the broader range of upper mantle melts. This also includes the olivines from Old Texcal Flow (which is negligibly affected by the slab flux). The Old Texcal Flow olivines have one of the lowest MnO and Mn/Fe of the arc front olivines, and are not transitional to the rear-arc olivines (Fig. 10a), which would be expected if the ambient arc front mantle was a subduction-modified variety of MORB/rear-arc mantle.

The fact that OIB-type and calc-alkaline/high-K olivines plot on one trend in olivine Fo-MnO-Mn/Fe space is consistent with their origin from a common mantle source. The general displacement of the calc-alkaline/high-K olivines to higher Fo and lower MnO relative is expected for the origin from a mantle that was depleted by previous melt extraction, given the constancy of the exchange coefficients ($KD^{Fe/Mg}_{oliv/melt}$ ~0.30; $KD^{Mn/Fe}_{oliv/melt}$ ~0.8). In a quantitative model, we assume that the originally fertile ambient prior to subduction modification produces melts that crystallize FeO- and MnO-rich olivines (~0.15 wt % MnO at Fo_{88}, Fig. 13, green star symbol). With increasing depletion, the residual mantle produces calc-alkaline/high-K melts with increasingly lower FeO and MnO, and higher Mg#, which crystallize olivines with higher Fo (Fo_{89}–Fo_{91}) and lower MnO (= 0.10–0.13 wt %), dependent on the extent of depletion (Fig. 13c, star symbols).

This effect of the ambient mantle depletion is also seen in the olivine Fo-Mn/Fe∗100 array. This array is much broader because olivine Mn/Fe is very sensitive to the inherent FeO and MnO variability of mantle melts. Primary melts of the TMVB arc front may easily crystallize olivines with Mn/Fe∗100 between ~1.38 and ~1.55. The slight increase of olivine Mn/Fe∗100 with decreasing Fo is only poorly matched by calculated olivine-only crystalline-of-descents (Fig. 13b and c), which suggests that the olivine Fo-MnO-Mn/Fe variability is derived from the mantle instead of being created by fractional crystallization. The inherent olivine Mn/Fe∗100 variability is enhanced by melt depletion: the models with the two representative calc-alkaline/high-K melts (Fig. 13d) shows that the melts from depleted mantle have slightly lower Mn/Fe ∗100 at higher Fo, because MnO is slightly more incompatible than FeO during mantle melting [$Kd^{Mn}_{oliv/melt} = \sim 0.8 * Kd^{Fe}_{oliv/melt}$; (Yu & Langmuir, 2023)] (Supplement C). Thus, the melts from the most depleted mantle have the lowest Mn/Fe∗100 in the liquidus olivines.

To summarize, we propose that the lower olivine Fo-MnO and Fo-Fe/Mn∗100 of the TMVB arc front magmas is due to melt origin from a mantle that is similar to the WPB mantle and that is variably depleted by previous slab flux-driven melt extraction.

Modeling results: olivine MnO-Ni variability

In Fig. 14, the olivine Ni and MnO models are recast into the olivine MnO vs Ni space. The ochre field outlines the WPB olivines normalized to Fo_{89} from Matzen *et al.* (2017) (see also Fig. 7). The individual olivine data points are now considered instead of high-Fo >88 olivine averages (Fig. 7), which shows that the TMVB olivines are consistent with melt origin from a heterogeneous mantle wedge that has been variably modified by slab flux-driven melt extraction. The least fluxed, fertile OIB-type mantle produces partial peridotite melts in equilibrium with higher olivine MnO, comparatively low-olivine Ni (but still higher than Ni in MORB olivines). The more strongly fluxed and depleted mantle produces the cooler, hydrous, and silicic calc-alkaline/high-K melts that crystallize high-Ni olivines above the MORB field with lower olivine MnO. Again, the very high-Ni olivines (~>4000 μg/g Ni) would require primary component melts with melt Ni enhanced by melt–rock reaction. Note that the steep increases in olivine Ni at near-constant olivine MnO above ~4000 μg/g Ni is consistent with the crystallization of very high-Ni olivines in melts with selectively increased melt Ni, while melt FeO, MgO, and MnO are buffered. Again, much of the high-Ni olivines with MnO >0.17 wt % (corresponding to olivines with ~<Fo88) could be produced by (recharge) melt mixing as the primary melts evolve further in the crust.

Implications for arc andesite formation in the TMVB

In summary, we propose that olivine Fo-Ni-MnO systematics in the TMVB are shaped by the cooler, more silicic and less magnesian primary melts formed by hydrous peridotite melting and melt-rock reaction processes in the mantle wedge. The mantle wedge is not homogeneous, but modified by 'subduction processing', which creates heterogeneity owing to the progressive depletion of the ambient mantle by slab flux-driven melt extraction combined with the selective reenrichment in slab-derived components (e.g. SiO_2, H_2O, alkalis, etc.) (e.g. Straub *et al.*, 2011*b*, 2015). This model was first inferred by bulk rock major and trace element and Sr-Nd-Pb-Hf isotope data from the same individual eruptive units of monogenetic and composite volcanoes studied here for olivine (Straub *et al.*, 2013, 2014, 2015). Notably, the olivine Fo-Ni-MnO systematics, together with the Cr-spinels, align with this model of subduction processing and refine it by adding new and unique information. The

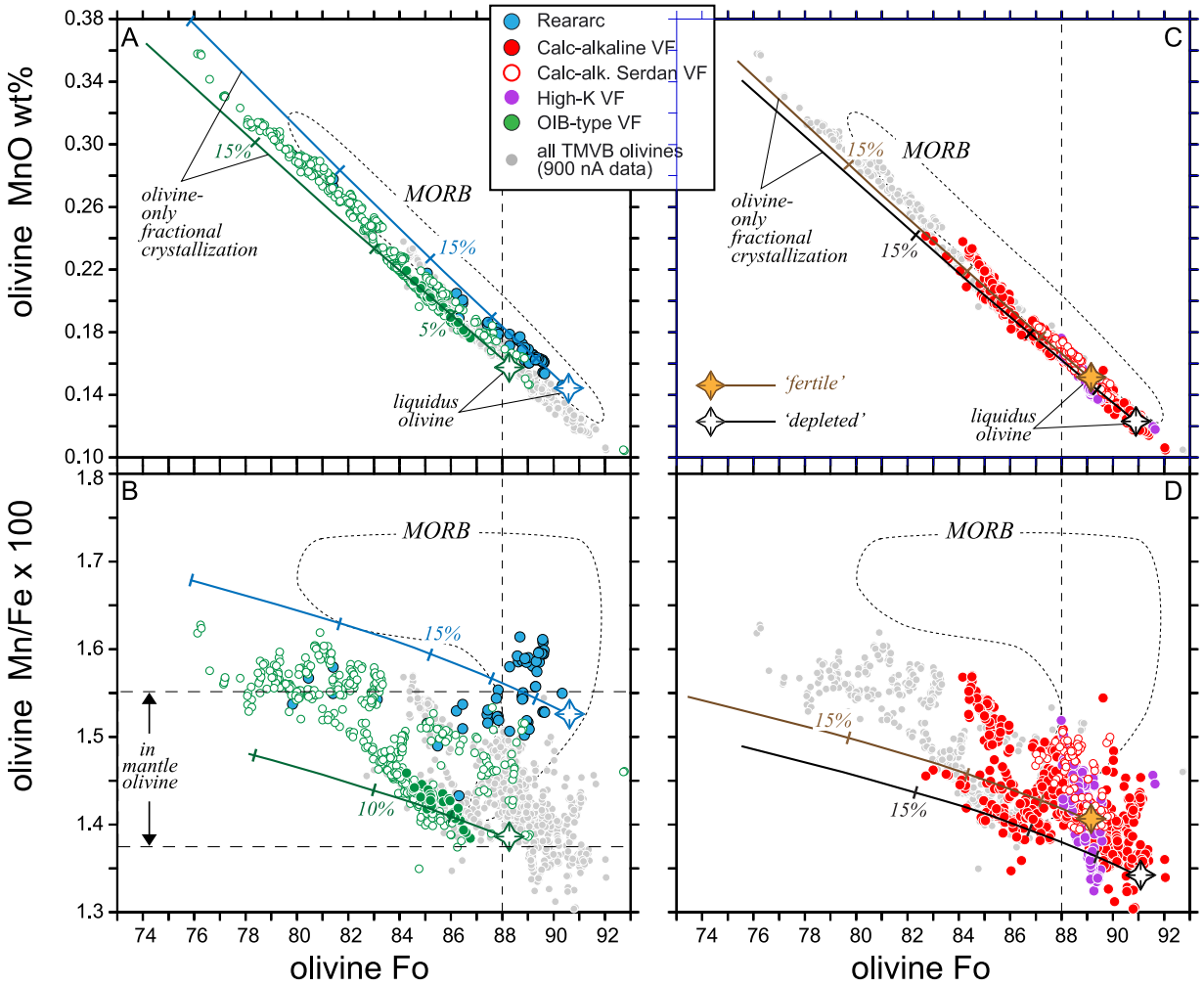

Fig. 13. Model results for olivine Fo vs MnO wt % and Fo vs Mn/Fe∗100 calculated with data in Table 1. Symbols as in Fig. 9. Olivine Fo-MnO—Mn/Fe∗100 are not sensitive to temperature. (a, b) Rear-arc and OIB-type arc front olivines, (c, d) calc-alkaline/high-K olivines.

striking dichotomy in olivine Fo-Ni and Fo-MnO behavior strongly indicates subduction processing because the divergent behavior of the Ni and MnO in the same olivines can only be explained by the interplay of melt temperature and composition (modulating Ni) and progressive mantle depletion (modulating MnO). Olivine Fo-Ni-MnO systematics confirm that a subduction-processed mantle wedge creates a broader range of primary melts. The olivine+Cr-spinels from the non-genetic melts reveal that primary melt silica increases as melt temperature decrease, the latter apparently being linked to the increasingly stronger (hydrous) slab flux (Fig. 5b). The olivine Fo-MnO trends provide crystal-scale evidence of the progressive mantle depletion, and in addition show that the TMVB arc front mantle is more akin to the enriched WPB mantle rather than to depleted MORB source. The olivine Ni is shaped by hydrous peridotite melting and by melt–rock reaction processes. Importantly, our results indicate that the Ni-rich component melts formed by melt–rock reaction could easily become diluted in the crust–mantle plumbing system before olivine crystallization, wiping out its record. This implies that melt–rock reaction processes in the mantle wedge may be more common in arc magmas than recognizable from the olivine Ni variations.

While the TMVB arc front olivines crystallize mostly non-cogenetic in melts, these melts still derive from a common mantle source (albeit diversified by subduction processing) and are incompletely hybridized en route to the surface. Thus, it is not unexpected that the Fo-Ni-MnO systematics of these olivines are molded into a semblance of coherency that often (but not always, see trends in olivine Fo-Mn/Fe∗100 space) resembles olivine fractionation trends. That does not mean that fractional crystallization plays no role at all: rather, fractional crystallization is part of the 'crustal overprinting' that additionally modifies the mantle melts by (recharge) melt mixing and hybridization before eruption. However, compared to the olivine diversity inherited from mantle melts, the influence of crustal overprinting appears to be much smaller.

Overall, our results show that the recycling of silicic slab components in the mantle wedge is essential for arc melt formation in the TMVB. In this context, the overall similarity of their WPB-thick olivine in olivine Fo-Ni-MnO space remains unexpected, considering that the WPB-thick primary melts are hotter, originate from greater mantle depths, and may not require melt–rock reaction to produce olivine variations. However, the similarity does not extend to the other olivine trace elements. For example, owing to their higher crystallization temperatures, the Hawaiian olivines (~WPB-thick) have twice as much $Al_2O_3 = 0.050 \pm 0.004$ wt % (Matthews *et al.*, 2021) as the TMVB calc-alkaline/high-K olivines ($Al_2O_3 = 0.024 \pm 0.007$ wt %). The Hawaiian olivines also have higher CaO = 0.271 ± 0.021 wt % than in the calc-alkaline/high-K TMVB olivines (CaO = 0.120 ± 0.23 wt %), which may be due to the higher melt CaO of the Hawaiian

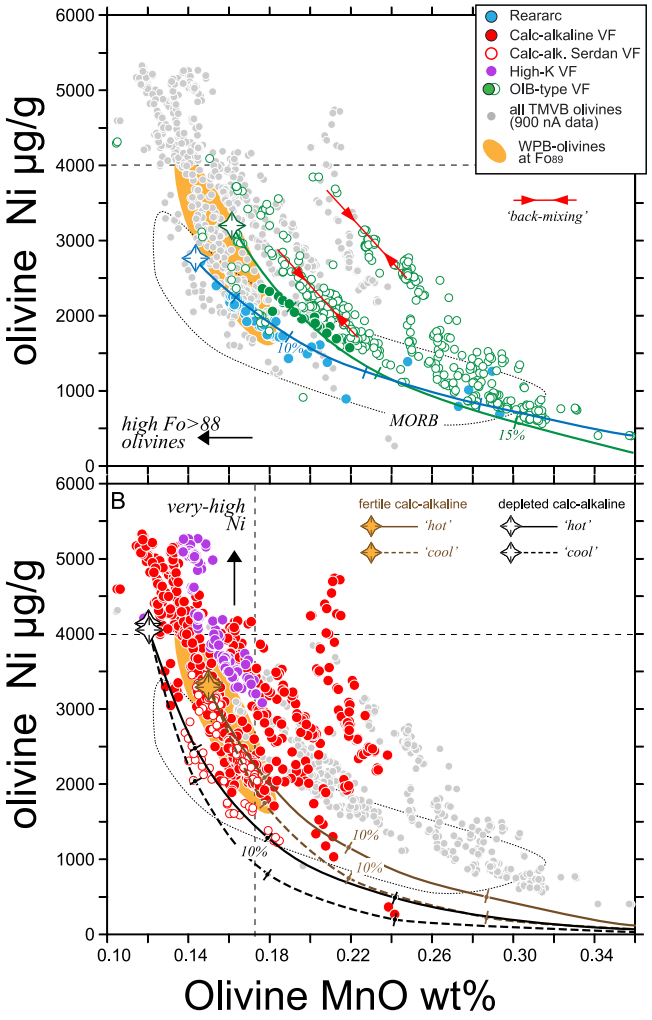

Fig. 14. Model results for olivine MnO wt % vs Ni µg/g calculated with data in Table 1. (**a**) Rear-arc and OIB-type olivines; (b) calc-alkaline/high-K olivines. Symbols and model curves as in Figs 9 and 13 Vertical stippled lines separate low-MnO olivine (with olivine Fo >88) from olivines with higher MnO (>0.17 wt %). Ochre field—WPB olivines normalized to Fo_{89} from Matzen *et al.* (2017). Double arrow-labeled 'back-mixing'—typically straight melt mixing trajectories caused (by recharge) melt mixing in the crust.

melts, either the hydrous nature of the TMVB melts, or a combination of both factors. Clearly, complete olivine trace element spectra are essential for understanding the processes of primary melt formation across different tectonic settings through their early-crystallizing olivines.

CONCLUSIONS

The following are the conclusions of this study:

- The Fo-Ni-MnO systematics of Cr-spinel-bearing olivines confirm that primary melts of the TMVB arc are more silicic, less magnesian, and cooler than the primary melts at mid-ocean ridges and in within-plate settings.
- While more silicic and cooler melts produced olivines with elevated Ni relative to MORB olivines, melt–rock reaction processes in the TMVB mantle wedge are needed to account for olivine with very high Ni contents (~>4000 µg/g).
- Olivine Fo-Ni-MnO systematics confirm an existing model inferred from bulk rock studies that primary TMVB melts are produced in a mantle wedge made heterogeneous by slab flux-driven melt extraction.
- The olivine Fo-MnO-Mn/Fe systematics suggest that the TMVB ambient mantle is similar to enriched WPB mantle and different from the depleted MORB source.
- Our study reaffirms a strong genetic link between slab recycling and arc andesite genesis.

SUPPLEMENTARY DATA

Supplementary data are available at *Journal of Petrology* online.

ACKNOWLEDGEMENTS

C. Kelso, C. Mandeville, K. Hammond, and C. Martin are thanked for their support during laboratory and analytical work.

FUNDING

This study was financially supported by the US National Science Foundation (grants EAR-19-21624 and -21643 to S.M.S. and E.W. and EAR-24-44123 to S.M.S.). Participation of V. Batanova and A. Sobolev and functioning of EPMA facility in ISTerre were supported by the grant from the European Research Council (ERC) under the European Union's Horizon H2020 research and innovation program (Synergy Grant MEET, grant agreement no.856555).

DATA AVAILABILITY

All new analytical data on the olivines are provided in Tables S1–S6 are accessible through the EarthChem Library of the Interdisciplinary Earth Data Alliance (IEDA): Straub *et al.* (2026), doi.org/10.60520/IEDA/113234.

REFERENCES

Ahmadi, J., Widom, E., Straub, S. M., Sanchez, R., Kuentz, D., Gómez-Tuena, A., Espinasa-Perena, R., Bindeman, I. N. & Stuart, F. M. (2025). Source vs. crustal processing in the trans-Mexican Volcanic Belt: constraints from Os-O-He isotope systematics in olivine. *Chemical Geology* **674**, 122574. https://doi.org/10.1016/j.chemgeo.2024.122574.

Beattie, P., Ford, C. & Russell, D. (1991). Partition coefficients for olivine-melt and orthopyroxene-melt systems. *Contributions to Mineralogy and Petrology* **109**, 212–224. https://doi.org/10.1007/BF00306480.

Beattie, P., Ford, C. & Russel, D. (1993). Partition coefficients for olivine-melt and orthopyroxene-melt systems (erratum). *Contributions to Mineralogy and Petrology* **114**, 288–288. https://doi.org/10.1007/BF00307763.

Blatter, D. L. & Burgess, S. D. (2025). Melt generation sources and conditions in the wake of a migrating slab window: geochemistry and petrology of the million-year history of primitive volcanism at Clear Lake volcanic field, California. *Journal of Petrology* **66**. https://doi.org/10.1093/petrology/egaf077.

Blatter, D. L. & Carmichael, I. S. E. (1998). Hornblende peridotites xenoliths from central Mexico reveal the highly oxidised nature of the subarc upper mantle. *Geology* **26**, 1035–1083. https://doi.org/10.1130/0091-7613(1998)026<1035:HPXFCM>2.3.CO;2.

Blatter, D. L., Farmer, G. L. & Carmichael, I. S. E. (2007). A north-south transect across the central Mexican Volcanic Belt at ca. 100oN: spatial distribution, petrological, geochemical and

isotopic characteristics or quaternary volcanism. *Journal of Petrology* **48**, 901–950. https://doi.org/10.1093/petrology/egm006.

Blatter, D. L., Sisson, T. W. & Hankins, W. B. (2013). Crystallization of oxidized, moderately hydrous arc basalt at mid-to lower-crustal pressures: implications for andesite genesis. *Contributions to Mineralogy and Petrology* **166**, 861–886. https://doi.org/10.1007/s00410-013-0920-3.

Bouvet de Maisonneuve, C., Costa, F., Huber, C., Vonlanthen, P., Bachmann, O. & Dungan, M. A. (2016). How do olivines record magmatic events? Insights from major and trace element zoning. *Contributions to Mineralogy and Petrology* **171**, 56. https://doi.org/10.1007/s00410-016-1264-6.

Brown Krein, S., Molitor, Z. J. & Grove, T. L. (2021). ReversePetrogen: a multiphase dry reverse fractional crystallization-mantle melting thermobarometer applied to 13,589 mid-ocean ridge basalt glasses. *Journal of Geophysical Research: Solid Earth* **126**, e2020JB021292. https://doi.org/10.1029/2020JB021292.

Bryant, J. A., Yogodzinksi, G. M. & Churikova, T. G. (2011). High-Mg# andesitic lavas of the Shisheisky complex, northern Kamchatka: implications for primitive calc-alkaline magmatism. *Contributions to Mineralogy and Petrology* **161**, 791–810. https://doi.org/10.1007/s00410-010-0565-4.

Cervantes, P. & Wallace, P. J. (2003a). The role of H2O in subduction zone magmatism: new insights from melt inclusions in high-Mg basalts from central Mexico. *Geology* **31**, 235–238. https://doi.org/10.1130/0091-7613(2003)031<0235:ROHOIS>2.0.CO;2.

Cervantes, P. & Wallace, P. J. (2003b). Magma degassing and basaltic eruption styles: a case study of V2000 year BP Xitle volcano in central Mexico. *Journal of Volcanology and Geothermal Research* **120**, 249–270. https://doi.org/10.1016/S0377-0273(02)00401-8.

Codillo, E. A., Le Roux, V. & Marschall, H. R. (2018). Arc-like magmas generated by mélange-peridotite interaction in the mantle wedge. *Nature Communications* **9**, 2864. https://doi.org/10.1038/s41467-018-05313-2.

Coogan, L. A., Saunders, A. D. & Wilson, R. N. (2014). Aluminum-in-olivine thermometry of primitive basalts: evidence of an anomalously hot mantle source for large igneous provinces. *Chemical Geology* **368**, 1–10. https://doi.org/10.1016/j.chemgeo.2014.01.004.

Díaz-Bravo, B. A., Gómez-Tuena, A., Ortega-Obregón, C. & Pérez-Arvizu, O. (2014). The origin of intraplate magmatism in the western trans-Mexican Volcanic Belt. *Geosphere* **10**, 340–373. https://doi.org/10.1130/GES00976.1.

Gavrilenko, M., Batanova, V. G., Llovet, X., Krasheninnikov, S., Koshlyakova, A. N. & Sobolev, A. V. (2023). Secondary fluorescence effect quantification of EPMA analyses of olivine grains embedded in basaltic glass. *Chemical Geology* **621**, 121328. https://doi.org/10.1016/j.chemgeo.2023.121328.

GeoROC (2024) *Geochemistry of Rocks of the Oceans and Continents*. Georg-August Universitaet Goettingen, Goettingen, Germany. https://georoc.eu/.

Gleeson, M. L. M. & Gibson, S. A. (2019). Crustal controls on apparent mantle pyroxenite signals in ocean-island basalts. *Geology* **47**, 321–324. https://doi.org/10.1130/G45759.1.

Gómez-Tuena, A., Orozco-Esquivel, M. T. & Ferrari, L. (2007) Igneous petrogenesis of the Trans-Mexican Volcanic Belt. In: Alaniz-Álvarez S. A. & Nieto-Samaniego Á. F. (eds) *Geology of México: Celebrating the Centenary of the Geological Society of México: Geological Society of America Special Paper 422*: 129–181. Boulder, Colorado USA.

Gómez-Tuena, A., Laura Mori, L., Goldstein, S. L. & Perez-Arvizu, O. (2011). Magmatic diversity of western Mexico as a function of metamorphic transformations in the subducted oceanic plate. *Geology* **75**, 213–241. 210.1016/j.gca.2010.1009.1029.

Gómez-Tuena, A., Díaz-Bravo, B., Vázquez-Duarte, A., Pérez-Arvizu, O. & Laura Mori, L. (2014) Andesite petrogenesis by slab-derived plume pollution of a continental rift. In: Gomez-Tuena A., Straub S. M. & Zellmer G. F. (eds) *Orogenic Andesite and Crustal Growth*. London: Geol Soc London Spec Pub 385, pp.65–101.

Gómez-Tuena, A., Mori, L. & Straub, S. M. (2018). Geochemical and petrological insights into the tectonic origin of the Transmexican Volcanic Belt. *Earth Science Reviews* **183**, 153–181. https://doi.org/10.1016/j.earscirev.2016.12.006.

Gordeychik, B., Churikova, T., Kronz, A., Sundermeyer, C., Simakin, A. & Wörner, G. (2018). Growth of, and diffusion in, olivine in ultra-fast ascending basalt magmas from Shiveluch volcano. *Scientific Reports* **8**, 11775. https://doi.org/10.1038/s41598-018-30133-1.

Hart, S. R. & Davis, K. E. (1978). Nickel partitioning between olivine and silicate melt. *Earth and Planetary Science Letters* **40**, 203–219. https://doi.org/10.1016/0012-821X(78)90091-2.

Heinrich, W. & Besch, T. (1992). Thermal history of the upper mantle beneath a young back-arc extensional zone: ultramafic xenoliths fron San Luis Potosi, Central Mexico. *Contributions to Mineralogy and Petrology* **111**, 126–142. https://doi.org/10.1007/BF00296583.

Herzberg, C., Asimow, P. D., Arndt, N., Niu, Y., Lesher, C. M., Fitton, J. G., Cheadle, M. J. & Saunders, A. D. (2007). Temperatures in ambient mantle and plumes: constraints from basalts, picrites, and komatiites. *Geochemistry, Geophysics, Geosystems* **8**. https://doi.org/10.1029/2006GC001390.

Jenner, F. E. & O'Neill, H. S. C. (2012). Analysis of 60 elements in 616 ocean floor basaltic glasses. *Geochemistry, Geophysics, Geosystems* **13**. https://doi.org/10.1029/2011GC004009.

Jennings, E. S., Gibson, S. A. & Maclennan, J. (2019). Hot primary melts and mantle source for the Paraná-Etendeka flood basalt province: new constraints from Al-in-olivine thermometry. *Chemical Geology* **529**, 119287. https://doi.org/10.1016/j.chemgeo.2019.119287.

Kelley, K. A. & Cottrell, E. (2009). Water and the oxidation state of subduction zone magmas. *Science* **325**, 605–6607. https://doi.org/10.1126/science.1174156.

Langmuir, C. H., Klein, E. M. & Plank, T. (1992) Petrological systematics of mid-ocean ridge basalts: constraints on melt generation beneath ocean ridges. In: Morgan J. P., Blackman D. K. & Sinton J. M. (eds) *Mantle Flow and Melt Generation at Mid-Ocean Ridges*. Washington: American Geophysical Union, pp.183–280.

Lara, M. & Dasgupta, R. (2020). Partial melting of a depleted peridotite metasomatized by a MORB-derived hydrous silicate melt—implications for subduction zone magmatism. *Geochimica et Cosmochimica Acta* **290**, 137–161. https://doi.org/10.1016/j.gca.2020.09.001.

Lee, C.-T. A., Luffi, P., Plank, T., Dalton, H. & Leeman, W. P. (2009). Constraints on the depths and temperatures of basaltic magma generation on Earth and other terrestrial planets using new thermobarometers for mafic magmas. *Earth and Planetary Science Letters* **279**, 20–33. https://doi.org/10.1016/j.epsl.2008.12.020.

Li, J., Huang, X.-L., Li, X.-H., Chu, F.-Y., Zhu, J.-H., Zhu, Z.-M. & Wang, H. (2021). Anomalously hot mantle source beneath the Dragon Flag supersegment of the southwest Indian ridge: new evidence from crystallisation temperatures of mid-ocean ridge basalts. *Lithos* **396-397**, 106221. https://doi.org/10.1016/j.lithos.2021.106221.

Luhr, J. F. & Gomez-Aranda, J. J. (1997). Mexican peridotite xenoliths and tectonic terranes: correlations among vent location, texture, temperature, pressure and oxygen fugacity. *Journal of Petrology* **38**, 1075–1112. https://doi.org/10.1093/petroj/38.8.1075.

Mallik, A., Nelson, J. & Dasgupta, R. (2015). Partial melting of fertile peridotite fluxed by hydrous rhyolitic melt at 2-3 GPa: implications for mantle wedge hybridization by sediment melt and generation of ultrapotassic magmas in convergent margins. *Contributions to Mineralogy and Petrology* **169**. https://doi.org/10.1007/s00410-015-1139-2.

Mallik, A., Dasgupta, R., Tsuno, K. & Nelson, J. (2016). Effects of water, depth and temperature on partial melting of mantle-wedge fluxed by hydrous sediment-melt in subduction zones. *Geochimica et Cosmochimica Acta* **195**, 226–243. https://doi.org/10.1016/j.gca.2016.08.018.

Matthews, S., Shorttle, O. & Maclennan, J. (2016). The temperature of the Icelandic mantle from olivine-spinel aluminum exchange thermometry. *Geochemistry, Geophysics, Geosystems* **17**, 4725–4752. https://doi.org/10.1002/2016GC006497.

Matthews, S., Wong, K., Shorttle, O., Edmonds, M. & Maclennan, J. (2021). Do olivine crystallization temperatures faithfully record mantle temperature variability? *Geochemistry, Geophysics, Geosystems* **22**, e2020GC009157. https://doi.org/10.1029/2020GC009157.

Matzen, A. K., Baker, M. B., Beckett, J. R. & Stolper, E. M. (2013). The temperature and pressure dependence of nickel partitioning between olivine and silicate melt. *Journal of Petrology* **54**, 2521–2545. https://doi.org/10.1093/petrology/egt055.

Matzen, A. K., Wood, B. J., Baker, M. B. & Stolper, E. M. (2017). The roles of pyroxenite and peridotite in the mantle sources of oceanic basalts. *Nature Geoscience* **10**, 530–535. https://doi.org/10.1038/ngeo2968.

Mitchell, A. L. & Grove, T. L. (2015). Melting the hydrous, subarc mantle: the origin of primitive andesites. *Contributions to Mineralogy and Petrology* **170**. https://doi.org/10.1007/s00410-00015-01161-00414.

Miyashiro, A. (1974). Volcanic rock series in island arcs and active continental margins. *American Journal of Science* **274**, 321–355. https://doi.org/10.2475/ajs.274.4.321.

Nimz, G. J., Cameron, K. I. & Niermayer, S. (1995). Formation of mantle lithosphere beneath the northern Mexico: chemical and Sr-Nd-Pb isotopic systematics of peridotite xenoliths from La Olivina. *Journal of Geophysical Research* **100**, 4181–4196. https://doi.org/10.1029/94JB02776.

Pardo, M. & Suarez, G. (1995). Shape of the subducted Rivera and Cocos plate in southern Mexico: seismic and tectonic implications. *Journal of Geophysical Research* **100**, 12357–12373. https://doi.org/10.1029/95JB00919.

Perez-Campos, X., Kim, Y. H., Husker, A., Davis, P. M., Clayton, R. W., Iglesias, A., Pacheco, J. F., Singh, S. K., Manea, V. C. & Gurnis, M. (2008). Horizontal subduction and truncation of the Cocos Plate beneath central Mexico. *Geophysical Research Letters* **35**, 18303. https://doi.org/10.1029/2008GL035127.

Pu, X., Lange, R. A. & Moore, G. M. (2024). Application of an improved olivine-melt thermometer/hygrometer to the Colima cone basanites and minettes of western Mexico: implications for the mantle source of unusually high-MgO melts. *Journal of Petrology* **65**. https://doi.org/10.1093/petrology/egad064.

Putirka, K. D. (2005). Mantle potential temperatures at Hawaii, Iceland, and the mid-ocean ridge system, as inferred from olivine phenocrysts: evidence for thermally driven mantle plumes. *Geochem Geophys Geosys* **6**. https://doi.org/10.1029/2005GC000915.

Putirka, K. D. (2008). Thermometers and barometers for volcanic systems. *Reviews in Mineralogy and Geochemistry* **69**, 61–120. https://doi.org/10.2138/rmg.2008.69.3.

Putirka, K. D., Ryerson, F. J., Perfit, M. R. & Ridley, W. I. (2011). Mineralogy and composition of the oceanic mantle. *Journal of Petrology* **52**, 279–313. https://doi.org/10.1093/petrology/egq080.

Rebaza Morillo, A. M., Mallik, A. & Straub, S. M. (2023). Multiple episodes of rock-melt reaction at the slab-mantle interface: formation of high silica primary magmas in intermediate to hot subduction zones. *Journal of Petrology* **64**, egad011. https://doi.org/10.1093/petrology/egad011.

Roberge, J., Delgado-Granados, H. & Wallace, P. J. (2009). Mafic magma recharge supplies high CO_2 and SO_2 gas fluxes from Popocatépetl volcano, Mexico. *Geology* **37**, 107–110. https://doi.org/10.1130/G25242A.1.

Ruprecht, P. & Plank, T. (2013). Feeding andesitic eruptions with a high-speed connection from the mantle. *Nature* **500**, 68–72. https://doi.org/10.1038/nature12342.

Schmidt, M. W. & Jagoutz, O. (2017). The global systematics of primitive arc melts. *Geochemistry, Geophysics, Geosystems* **18**, 2817–2854. https://doi.org/10.1002/2016GC006699.

Sobolev, A. V., Hofmann, A. W., Sobolev, V. S. & Nikogosian, I. K. (2005). An olivine-free mantle source of Hawaiian shield basalts. *Nature* **434**, 590–597. https://doi.org/10.1038/nature03411.

Sobolev, A. V., Hofmann, A. W., Kuzmin, D. V., Yaxley, G. M., Arndt, N. T., Chung, S. L., Danyushevsky, L. V., Elliott, T., Frey, F. A., Garcia, M. O., Gurenko, A. A., Kamenetsky, V. S., Kerr, A. C., Krivolutskaya, N. A., Matvienkov, V. K., Nikogosian, I. K., Rocholl, A., Sigurdsson, I. A., Sushchevkaya, N. M. & Teklay, M. (2007). The amount of recycled crust in sources of mantle-derived melts. *Science* **316**, 412–417. https://doi.org/10.1126/science.1138113.

Spice, H. E., Fitton, J. G. & Kirstein, L. A. (2016). Temperature fluctuation of the Iceland mantle plume through time. *Geochemistry, Geophysics, Geosystems* **17**, 243–254. https://doi.org/10.1002/2015GC006059.

Straub, S. M. & Martin-Del Pozzo, A. L. (2001). The significance of phenocryst diversity in tephra from recent eruptions at Popocatepetl volcano (central Mexico). *Contributions to Mineralogy and Petrology* **140**, 487–510. https://doi.org/10.1007/PL00007675.

Straub, S. M., LaGatta, A. B., Martin-Del Pozzo, A. L. & Langmuir, C. H. (2008). Evidence from high Ni olivines for a hybridized peridotite/pyroxenite source for orogenic andesites from the central Mexican Volcanic Belt. *Geochem Geophys Geosys* **9**, Q03007. https://doi.org/10.1029/2007GC001583.

Straub, S. M., Gomez-Tuena, A., Stuart, F. M., Zellmer, G. F., Cai, M. Y. & Espinasa-Perena, R. (2011a) *High-Ni Olivines and the Mantle Origin of Arc Andesites*. Melbourne, Australia: XXV IUGG General Assembly.

Straub, S. M., Gomez-Tuena, A., Stuart, F. M., Zellmer, G. F., Espinasa-Perena, R., Cai, M. Y. & Iizuka, Y. (2011b). Formation of hybrid arc andesites beneath thick continental crust. *Earth and Planetary Science Letters* **303**, 337–347. https://doi.org/10.1016/j.epsl.2011.01.013.

Straub, S. M., Gomez-Tuena, A., Zellmer, G. F., Espinasa-Perena, R., Stuart, F. M., Cai, Y., Langmuir, C. H., Martin-Del Pozzo, A. & Mesko, G. T. (2013). The processes of melt differentiation in arc volcanic rocks: insights from OIB-type arc magmas in the central Mexican Volcanic Belt. *Journal of Petrology* **54**, 665–701. https://doi.org/10.1093/petrology/egs081.

Straub, S. M., Zellmer, G. F., Gómez-Tuena, A., Espinasa-Perena, R., Martin-Del Pozzo, A. L., Stuart, F. M. & Langmuir, C. H. (2014) A genetic link between silicic slab components and calc-alkaline arc volcanism in central Mexico. In: Gomez-Tuena A., Straub S. M. & Zellmer G. F. (eds) *Orogenic Andesites and Crustal Growth. The Geological Society of London, Geol Soc London Spec Pub* 385, pp.31–64.

Straub, S. M., Gomez-Tuena, A., Bindeman, I. N., Bolge, L. L., Brandl, P. A., Espinasa-Perena, R., Solari, L., Stuart, F. M., Vannucchi, P. &

Zellmer, G. F. (2015). Crustal recycling by subduction erosion in the central Mexican Volcanic Belt. *Geology* **166**, 29–52.

Straub, S. M., Batanova, V., Sobolev, A., Gómez-Tuena, A., Espinasa-Perena, R., Fleming, W. L., Bindeman, I. N., Stuart, F. M., Widom, E. & Iizuka, Y. (2023). The systematics of olivine CaO + Cr-spinel in high-Mg# arc volcanic rocks: evidence for in-situ mantle wedge depletion at the arc volcanic front. *Journal of Petrology* **64**. https://doi.org/10.1093/petrology/egad085.

Straub, S. M., Batanova, V., Sobolev, A. V., Gomez-Tuena, A., Espinasa-Perena, R., Fleming, W. L., Bindeman, I. N., Stuart, F. M., Widom, E. & Iizuka, Y. (2026) Olivine and Cr-spinel major and trace elements, olivine He and O isotope data and major and trace elements of bulk rocks from quaternary volcanic rocks from the Trans-Mexican Volcanic Belt, Version 1.0. In: (IEDA), I. E. D. A (ed) *Interdisciplinary Earth Data Alliance (IEDA)*.

Tenner, T. J., Hirschmann, M. M. & Humayun, M. (2012). The effect of H2O on partial melting of garnet peridotite at 3.5 GPa. *Geochemistry, Geophysics, Geosystems* **13**. https://doi.org/10.1029/2011GC003942.

Till, C. B. (2017). A review and update of mantle thermobarometry for primitive arc magmas. *American Mineralogist* **102**, 931–947.

Trela, J., Gazel, E., Sobolev, A. V., Moore, L., Bizimis, M., Jicha, B. & Batanova, V. G. (2017). The hottest lavas of the Phanerozoic and the survival of deep Archaean reservoirs. *Nature Geoscience* **10**(451), 451–456. https://doi.org/10.1038/ngeo2954.

Ulmer, P., Kaegi, R. & Müntener, O. (2018). Experimentally derived intermediate to silica-rich arc magmas by fractional and equilibrium crystallization at 1·0 GPa: an evaluation of phase relationships, compositions, liquid lines of descent and oxygen fugacity. *Journal of Petrology* **59**, 11–58. https://doi.org/10.1093/petrology/egy017.

Veter, M., Foley, S. F., Mertz-Kraus, R. & Groschopf, N. (2017). Trace elements in olivine of ultramafic lamprophyres controlled by phlogopite-rich mineral assemblages in the mantle source. *Lithos* **292-293**, 81–95. https://doi.org/10.1016/j.lithos.2017.08.020.

Wallace, P. J. & Carmichael, I. S. E. (1999). Quaternary volcanism near the valley of Mexico: implications for subduction zone magmatism and the effects of crustal thickness variations on primitive magma compositions. *Contributions to Mineralogy and Petrology* **135**, 291–314. https://doi.org/10.1007/s004100050513.

Wang, Z. & Gaetani, G. A. (2008). Partitioning of Ni between olivine and siliceous eclogite partial melt: experimental constraints on the mantle source of Hawaiian basalts. *Contributions to Mineralogy and Petrology* **156**, 661–678. https://doi.org/10.1007/s00410-008-0308-y.

Weaver, S. L., Wallace, P. J. & Johnston, D. A. (2011). A comparative study of continental vs. intraoceanic arc mantle melting: experimentally determined phase relations of hydrous primitive melts. *Earth and Planetary Science Letters* **308**, 97–106. https://doi.org/10.1016/j.epsl.2011.05.040.

Weber, R. M., Wallace, P. J. & Johnston, A. D. (2011). Experimental insights into the formation of high-Mg basaltic andesites in the Trans-Mexican Volcanic Belt. *Contributions to Mineralogy and Petrology* **163**, 825–840.

Wu, Y.-D., Yang, J.-H., Stagno, V., Nekrylov, N., Wang, J.-T. & Wang, H. (2022). Redox heterogeneity of picritic lavas with respect to their mantle sources in the Emeishan large igneous province. *Geochimica et Cosmochimica Acta* **320**, 161–178. https://doi.org/10.1016/j.gca.2022.01.001.

Xu, R. & Liu, Y. (2016). Al-in-olivine thermometry evidence for the mantle plume origin of the Emeishan large igneous province. *Lithos* **266-267**, 362–366. https://doi.org/10.1016/j.lithos.2016.10.016.

Yang, S., Humayun, M. & Salters, V. J. M. (2018). Elemental systematics in MORB glasses from the mid-Atlantic ridge. *Geochemistry, Geophysics, Geosystems* **19**, 4236–4259. https://doi.org/10.1029/2018GC007593.

Yu, M. & Langmuir, C. H. (2023). The origin of Ni and Mn variations in Hawaiian and MORB olivines and associated basalts. *Chemical Geology* **640**, 121745. https://doi.org/10.1016/j.chemgeo.2023.121745.

Zhang, L., Ren, Z.-Y., Zhang, L., Wu, Y.-D., Qian, S.-P., Xia, X.-P. & Xu, Y.-G. (2021). Nature of the mantle plume under the Emeishan large igneous province: constraints from olivine-hosted melt inclusions of the Lijiang picrites. *Journal of Geophysical Research: Solid Earth* **126**, e2020JB021022. https://doi.org/10.1029/2020JB021022.

Zhang, Y., Namur, O., Li, W., Shorttle, O., Gazel, E., Jennings, E., Thy, P., Grove, T. L. & Charlier, B. (2023). An extended calibration of the olivine–spinel aluminum exchange thermometer: application to the melting conditions and mantle lithologies of large igneous provinces. *Journal of Petrology* **64**. https://doi.org/10.1093/petrology/egad077.

Journal of Petrology, 2025, **66**, egaf094
https://doi.org/10.1093/petrology/egaf094
Original Manuscript